CELL BIOLOGY

ASPL couples the assembly of stress granules with their VCP-mediated disassembly

Gautam Pareek[1]†, Dongfang Li[1]†, Bo Wang[2,3]*†, Jinjun Wu[1], Brian D. Freibaum[1], Joseph L. Basalla[4], Tharun Selvam Mahendran[4], Anurag Singh[4], Amanda Nourse[5], Honghu Quan[1]‡, Ravi Kalathur[5], Mitra S. Rana[5], Brian Maxwell[1], Yong-Dong Wang[1], James Messing[1], Yonghui Ni[6], Stanley Pounds[6], Rachayata Dharmat[1], Jingjun Lu[1], Xiujie Li-Harms[1], Alexandre F. Carisey[1], Shondra M. Pruett-Miller[1,7], J. Paul Taylor[1], Priya Banerjee[4], Hong Joo Kim[1], Mondira Kundu[1]*

Stress granules (SGs) are dynamic RNA-protein assemblies that form in response to cellular stress and must be efficiently disassembled to restore normal cell function. Valosin-containing protein (VCP), an enzyme implicated in neurodegenerative diseases, is essential for SG disassembly, but whether and how this process is coordinated with SG assembly remains unclear. Here, we identify the VCP cofactor, Alveolar soft part sarcoma locus (ASPL) as a key regulator linking SG assembly and disassembly. ASPL promotes SG assembly by facilitating biomolecular condensation of Ras guanosine triphosphatase–activating protein-binding protein (G3BP) and stabilizing its interactions with other SG proteins. ASPL also facilitates phosphorylation and activation of VCP by UNC-51-like kinases 1 and 2 (ULK1/2), enabling G3BP extraction and efficient SG disassembly. Pathogenic VCP mutations that disrupt ASPL binding impair SG disassembly, a defect rescued by phosphomimetic mutations or ASPL depletion. Our findings suggest that disruptions in the ASPL-VCP interaction uncouple SG assembly and disassembly, representing a potential mechanism underlying VCP-associated neurodegenerative diseases.

INTRODUCTION

Stress granules (SGs) are transient ribonucleoprotein (RNP) assemblies that form in response to acute cellular stresses that stall translation (*1*, *2*). Removal of stress typically leads to resolution of SGs by disassembly (*3*–*6*). SGs are among a growing number of biologically relevant condensates whose formation depends on liquid-liquid phase separation (LLPS), a type of phase transition in which molecules in a single diffuse phase demix into a dense phase and a dilute phase (*7*–*9*). The SG itself constitutes the dense phase, where RNA and proteins are concentrated, and the surrounding cytoplasm corresponds to the dilute phase, where these molecules are relatively depleted. As prototypical RNP assemblies, SGs are composed of RNAs and proteins that engage in weak and multivalent protein-protein, protein-RNA, and RNA-RNA interactions (*10*–*16*). Once the sum of these interactions breaches a particular threshold (e.g., the condensation threshold), a system-spanning network is formed and gives rise to a phase transition by separating the granule from its surroundings (*8*, *17*, *18*). Conversely, when the network of interactions falls below this threshold, the granule disassembles in a reversal of LLPS. Among the key factors influencing condensation thresholds are the concentration of relevant biomolecules (e.g., nucleic acids and proteins), the number of interactions per molecule, the strength of interactions between the molecules, and the diffusion timescales of the molecules. In the context of SG assembly, two such relevant biomolecules are G3BP1 (Ras guanosine triphosphatase–activating protein-binding protein 1, hereafter referred to as G3BP) and G3BP2, redundant RNA binding proteins that occupy nodes with the highest centrality in the SG interaction network (*14*). The RNA-dependent condensation of G3BP is a major driver of SG assembly, and G3BP-interacting partners can influence SG dynamics by altering the SG condensation threshold (*14*–*16*).

Although the precise functions of SGs are still not fully understood, recent studies have shown that the composition and interaction networks of individual RNP granules including SGs can influence their roles and dynamic behaviors (*19*–*25*). Notably, several proteins found in SGs are encoded by genes that are frequently mutated in patients with multisystem proteinopathy (MSP) and related disorders such as amyotrophic lateral sclerosis, frontotemporal dementia, and inclusion body myopathy (IBM) (*10*–*13*). When expressed in cultured cells, these mutated proteins can slow the dynamics of SGs and other RNP assemblies, leading to persistent TDP43+ granules and/or the formation of rigid, amyloid-like solids reminiscent of those observed in affected tissues of patients with MSP and related disorders (*26*–*31*). Similarly, animal models expressing these disease-associated mutations develop TDP43+ pathology (*26*, *32*–*38*). These observations have contributed to the prevailing view that MSP and related disorders arise from perturbations in protein homeostasis and RNA metabolism, often linked to aberrant phase transitions that contribute to the abnormal accumulation of inclusions that stain positive for ubiquitin, SQSTM1, TDP43, and other RNP granule components (*26*, *39*–*43*).

Mutations in the gene encoding VCP (valosin-containing protein) are the most common cause of MSP, a pleiotropic disorder diagnosed when patients or families exhibit symptoms of at least two

[1]Department of Cell and Molecular Biology, St. Jude Children's Research Hospital, Memphis, TN, USA. [2]State Key Laboratory of Cellular Stress Biology, School of Life Sciences, Faculty of Medicine and Life Sciences, Xiamen University, Xiamen, China. [3]Shenzhen Research Institute of Xiamen University, Shenzhen, China. [4]Department of Physics, The State University of New York at Buffalo, Buffalo, NY, USA. [5]Department of Structural Biology, St. Jude Children's Research Hospital, Memphis, TN, USA. [6]Department of Biostatistics, St. Jude Children's Research Hospital, Memphis, TN, USA. [7]Center for Advanced Genome Engineering, St. Jude Children's Research Hospital, Memphis, TN, USA.
*Corresponding author. Email: mondira.kundu@stjude.org (M.K.); bowang@xmu.edu.cn (B.W.)
†These authors contributed equally to this work.
‡Present address: Neurocrine Biosciences, San Diego, CA, USA.

of the following conditions: amyotrophic lateral sclerosis, frontotemporal dementia, IBM, or Paget's disease of bone. VCP is a multifunctional AAA adenosine triphosphatase (ATPase) that forms a hexamer and participates in various cellular processes, including endoplasmic reticulum–associated protein degradation and autophagy (*44*–*47*). Its activity is regulated by a validated suite of interacting proteins, which function either as adapters linking VCP to specific substrates or as direct modulators of its activity (*3*–*5*, *48*). Among VCP's cofactors is ASPL (alveolar soft part sarcoma locus), also referred to as ASPSCR1 (alveolar soft part sarcoma chromosomal region candidate gene 1), TUG [tether containing UBX (ubiquitin regulatory X) domain for GLUT4 (glucose transporter type 4)], and UBXD9 (UBX domain–containing protein 9) (*48*–*51*). ASPL is thought to negatively regulate VCP's activity by disrupting its hexameric structure (*52*). Beyond its role as a VCP cofactor, ASPL is also involved in glucose metabolism, where it regulates the insulin-stimulated translocation of GLUT4 from intracellular storage vesicles to the plasma membrane, a process crucial for glucose uptake in adipose tissue and muscle cells (*53*). ASPL dysfunction has been implicated in cancer, where it forms a characteristic fusion with transcription factor E3 (*51*, *54*). However, the extent of the functional overlap between ASPL and VCP-related functions is not clear; it is not known whether ASPL regulates specific subsets of VCP-related functions, and, conversely, VCP's role in functions ascribed to ASPL has not been delineated.

Although not considered a core SG constituent, VCP is recruited to SGs, where it contributes to their disassembly by extracting SG proteins, such as G3BP (*3*, *4*). Furthermore, expression of MSP-associated mutations in VCP leads to the accumulation of dynamically arrested SGs (*27*). Certain disease-associated VCP mutations that drive the accumulation of poorly dynamic SGs may also influence VCP's interaction with ASPL (*55*, *56*); however, whether ASPL or its interaction with VCP contributes to SG dynamics has not been examined. In this study, we aimed to define the functions of ASPL in SG dynamics and their relevance to MSP. We found that ASPL has a direct role in regulating RNP granule dynamics by coupling the assembly and disassembly of SGs. Specifically, we found that ASPL promotes SG assembly by stabilizing interactions among core SG proteins, including G3BP, thus reducing the threshold for condensation. Conversely, we found that ASPL supports efficient SG disassembly by facilitating the phosphorylation and activation of VCP by the serine-threonine kinase ULK1/2. These findings provide key insights into the molecular mechanisms governing SG dynamics and shed light on how specific VCP mutations may lead to the aberrant persistence of RNP granules, which are thought to underlie the pathogenesis of MSP and related disorders. Our improved understanding of the assembly and disassembly of SGs will lay the groundwork to pursue meaningful therapeutic treatments for MSP and related disorders in the future.

RESULTS

ASPL is required for the efficient assembly and disassembly of SGs

To determine whether ASPL is involved in regulating SG dynamics, we first examined the subcellular distribution of ASPL before and after subjecting cells to heat shock (HS) or sodium arsenite (SA) treatment, both of which are potent inducers of SG formation (*14*). To facilitate the detection of endogenous ASPL, we used CRISPR-Cas9 to tag the N or C terminus of endogenous ASPL with 3×-FLAG. Using these knock-in cell lines, we found that ASPL colocalized with the SG marker TIAR (T cell intracellular antigen 1–related protein) in cells subjected to either treatment (fig. S1, A to D).

Next, we tested the effects of altering ASPL expression on SG dynamics. First, we found that transiently overexpressing wild-type (WT) green fluorescent protein (GFP)–tagged ASPL (to levels >3-fold higher than endogenous ASPL) in HeLa cells grown under standard culture conditions (i.e., without any additional treatments) increased the percentage of cells harboring G3BP+ and TIAR+ granules (Fig. 1, A and B, and fig. S1E). These granules were also positive for GFP-ASPL and several other SG markers, such as eIF3η, TDP43, TIA1, and PABP1 (Fig. 1A). This increase in spontaneous SG-like assemblies may result from promoting their formation and/or impairing their disassembly. Given that ASPL has been implicated as a negative regulator of VCP (*52*) and VCP activity is required for SG disassembly (*3*, *4*), we hypothesized that the disruption of VCP function contributes to the accumulation of spontaneous SG-like assemblies. To test this hypothesis, we overexpressed mutant forms of GFP-ASPL containing alanine substitutions of aspartate-351 (D351A) or proline-437 and proline-438 (PPAA), key residues involved in mediating the interaction with VCP (*52*). These mutant forms of ASPL not only failed to interact with VCP (fig. S1F) but also failed to disrupt VCP hexamers when overexpressed in cells (fig. S1G), as previously described (*52*). Nevertheless, when overexpressed at levels comparable to WT GFP-ASPL in transiently transfected HeLa cells, these VCP binding–defective forms of ASPL were as effective as WT GFP-ASPL in promoting the spontaneous accumulation of SG-like assemblies (Fig. 1B and fig. S1H), indicating that this function of ASPL does not rely on its ability to interact with and/or disrupt VCP hexamers.

We next investigated the role of endogenous ASPL in SG formation using RNA interference (RNAi)–mediated silencing in cells subjected to HS or SA. Compared to cells treated with a nontargeting control siRNA (siCtrl), silencing of endogenous *ASPL* by siRNA (si*ASPL*) reduced the area of puncta occupied by various SG proteins, including G3BP, TIAR, eIF3η, and PABP1 (Fig. 1, C and D, and fig. S1, I to K). We further analyzed ASPL's role in SG dynamics using live-cell and static imaging in U2OS cells expressing endogenous G3BP tagged with tdTomato (*14*). *ASPL* depletion again caused defects in SG assembly under both HS (Fig. 1, E to G) and SA (Fig. 1, H and I) stress conditions. These defects were rescued in cells stably expressing RNAi-resistant WT GFP-ASPL at levels similar to endogenous ASPL (Fig. 1, E to I; fig. S1, L and M; table S1A; and movie S1). We also examined the ability of the stably expressed VCP binding–defective mutants to rescue the defect in SG assembly caused by RNAi-mediated *ASPL* knockdown. Immunoblot and fluorescence-activated cell sorting analyses confirmed comparable expression of WT ASPL and VCP binding–defective mutants in U2OS cells (fig. S1, M to P). Although cells expressing D351A or PPAA ASPL mutants showed normal SG assembly in response to HS or SA treatment, they exhibited impaired disassembly (Fig. 1, E to I; table S1A; and movie S1), similar to that caused by pharmacologic or genetic inhibition of VCP (*3*–*5*, *57*). This indicates that ASPL is required for both the efficient assembly and disassembly of SGs. Moreover, although interaction with VCP is not essential for ASPL's role in SG assembly, it is crucial for the efficient disassembly of SGs upon removal of inciting stressors.

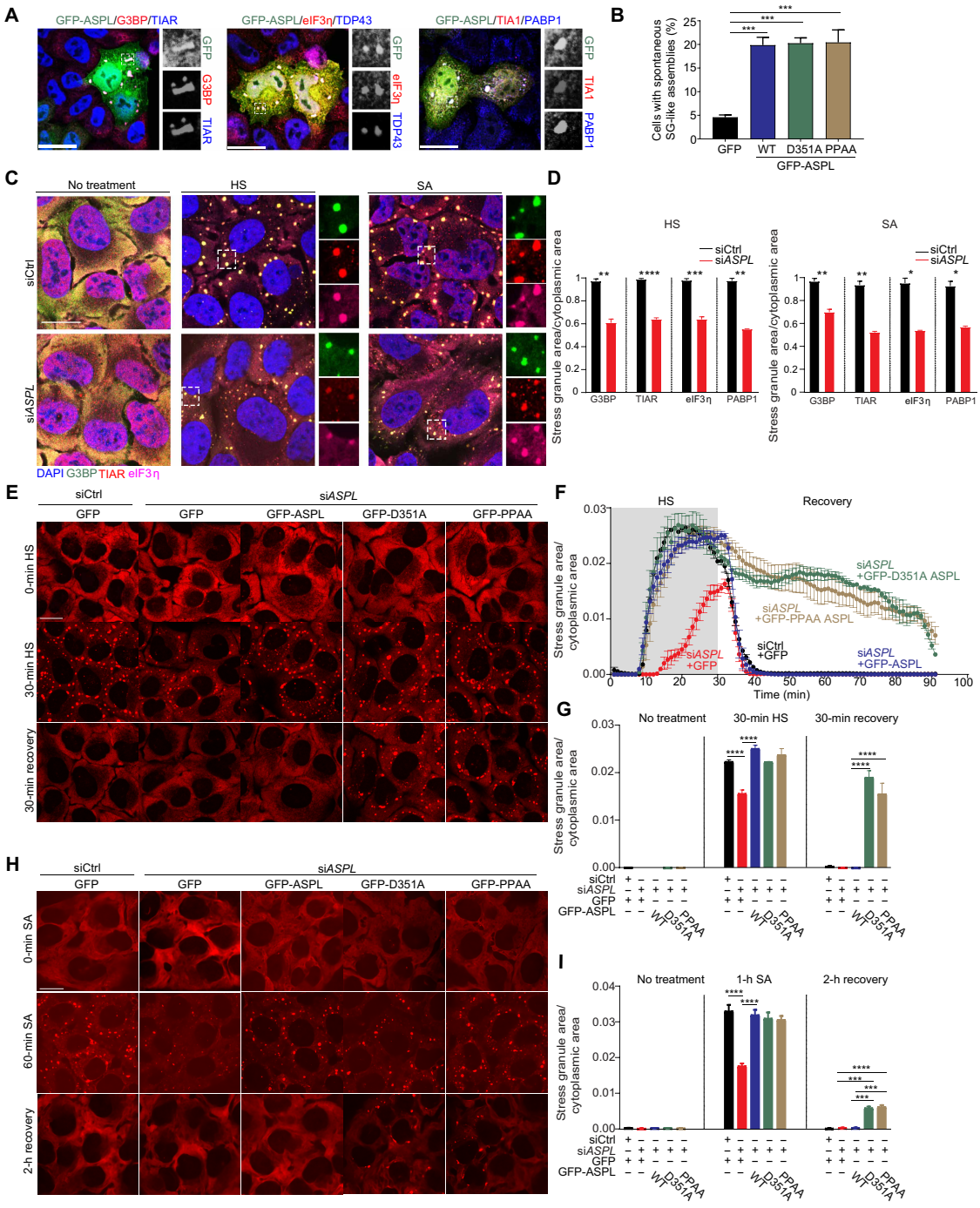

Fig. 1. ASPL regulates SG assembly and disassembly in cells. (**A**) HeLa cells were transfected with plasmid expressing GFP-ASPL and stained. Images highlight colocalization of GFP-ASPL with SG markers. (**B**) Percentage of HeLa cells containing SG-like assemblies in cells expressing indicated constructs. $n > 100$ cells from three biological replicates. $^{***}P \leq 0.001$ by analysis of variance (ANOVA) with Tukey's test. (**C** and **D**) U2OS cells transfected with nontargeting small interfering RNA (siRNA) (siCtrl) or si*ASPL* were subjected to 60-min HS treatment at 43°C or 500 μM SA treatment for 60 min and then stained for SG markers. (C) Merged images. (D) Ratio of SG area to cytoplasmic area for each antibody. $^{*}P \leq 0.05$, $^{**}P \leq 0.01$, $^{***}P \leq 0.001$, and $^{****}P \leq 0.0001$ by Student's *t* test. (**E**) Live-cell imaging of G3BP-tdTomato knock-in U2OS cells stably expressing GFP, si*ASPL*-resistant GFP-ASPL, GFP-D351A ASPL, or GFP-PPAA ASPL, along with siCtrl or si*ASPL*. Cells were subjected to HS, followed by 1-hour (h) recovery at 37°C. (**F**) Area occupied by SGs normalized to cytoplasmic area as shown in (E). (**G**) Area occupied by SGs normalized to cytoplasmic area in cells, as shown in (E), before HS, after 30 min of HS, and after 30 min of recovery. $n > 60$ cells from a representative experiment. $^{****}P \leq 0.0001$ by ANOVA with Tukey's test. (**H**) Fixed cell images of G3BP-tdTomato knock-in U2OS cells stably expressing GFP, si*ASPL*-resistant GFP-ASPL, GFP-D351A ASPL, or GFP-PPAA ASPL along with siCtrl or siRNA against *ASPL* after 1-hour 500 μM SA treatment, followed by 2-hour recovery at 37°C. (**I**) Area occupied by SGs normalized to cytoplasmic area in cells as shown in (H) before SA treatment, after 1-hour SA treatment, and after 2-hour recovery. $n > 100$ cells from two biological replicates. $^{***}P \leq 0.001$ and $^{****}P \leq 0.0001$ by ANOVA with Tukey's test. Scale bars, 20 μm. Data are presented as means ± SEM.

ASPL lowers the threshold concentration of G3BP required for condensation in cells and lysates

SG formation can be promoted or inhibited by modulating the core SG interaction network, where G3BP1/2 occupies the central node and plays an essential role in the assembly of SGs in response to certain stressors (*14*–*16*, *58*). As reported previously (*14*), SGs are completely absent from SA-treated *G3BP1/2* double-knockout (DKO) cells but are occasionally noted in DKO cells subjected to HS (fig. S2A). Nevertheless, the area occupied by SGs (marked by TIAR or eIF3η) in DKO cells treated with either stressor was markedly and significantly ($P < 0.0001$) reduced compared to that in WT cells (fig. S2, A and B), highlighting the importance of G3BP in the efficient assembly of SGs under both conditions. Given G3BP's central role in SG assembly, intracellular phase separation thresholds relevant for SG assembly can be measured by determining the threshold concentration of G3BP required for SG formation. Reexpressing G3BP1 in *G3BP1/2* DKO cells leads to the formation of SGs that are positive for a variety of different SG proteins in a manner that is dependent on the amount of G3BP expressed in each cell (*14*). By relating the extent of SG assembly to the amount of G3BP expressed per cell, one can determine the probability of SG formation at a given G3BP concentration (Fig. 2A). We used this system to assess whether ASPL promotes SG assembly by influencing the threshold concentration of G3BP required for SG formation.

First, we transiently transfected GFP-G3BP into *G3BP1/2* DKO cells with either siCtrl or si*ASPL*. We then quantified the total amount of G3BP in the transfected cells with or without SGs to determine the probability of SG formation in untreated cells or cells treated with SA. Under basal conditions, the probability of SG formation in relation to G3BP concentration was only minimally affected by *ASPL* knockdown (Fig. 2B and fig. S2C). However, in cells treated with SA, *ASPL* knockdown significantly ($P < 0.001$) decreased the probability of SG formation as a function of G3BP concentration (Fig. 2C and fig. S2D). These findings suggest that decreased levels of ASPL reduced the likelihood of stress-induced SG formation by increasing the threshold concentration of G3BP required for condensation.

Just as the overexpression of G3BP drives the formation of SGs in cells, condensates with protein compositions akin to SGs can be reconstituted in cellular lysates by adding recombinant G3BP (*59*). To determine whether ASPL promotes G3BP condensation, we introduced increasing concentrations of purified recombinant ASPL into lysates prepared from cells stably expressing G3BP-GFP and monitored droplet formation using microscopy (Fig. 2D). This led to the formation of G3BP-GFP+ phase-separated droplets at ASPL concentrations as low as 10 μM, with the total droplet area increasing in a concentration-dependent manner (Fig. 2, E and F, and fig. S2, E and F). Using lysates spiked with fluorescently labeled ASPL or oligo(dT) primers, we detected the enrichment of ASPL and mRNA signals in the ASPL-induced G3BP-GFP+ droplets (fig. S2G). We also observed the recruitment of other SG components (e.g., TIA1, caprin 1, and TDP43) into ASPL-induced droplets using lysates from cells expressing fluorescently tagged versions of those proteins generated through CRISPR-Cas9–mediated knock-in (fig. S2H). The staining patterns were similar to those observed with the droplets induced by the addition of G3BP (*59*).

To further investigate the protein composition of ASPL-induced droplets, we analyzed and compared the proteins in condensates formed by recombinant ASPL or G3BP to those in an unseeded U2OS lysate using liquid chromatography–tandem mass spectrometry (LC-MS/MS). We identified 556 proteins enriched in ASPL-induced granules and 310 proteins enriched in G3BP-induced granules, with 239 proteins showing more than threefold enrichment in both types of droplets (fig. S2I and table S1B). Gene ontology (GO) analysis revealed that proteins common to both ASPL- and G3BP-induced droplets were highly enriched for constituents of RNP complexes, including those found in cytoplasmic SGs (fig. S2J and table S1C). This suggests that when introduced into cellular lysates, ASPL can promote the formation of phase-separated condensates enriched in G3BP and other SG-associated proteins.

Given the central role of G3BP in SG assembly, we next investigated whether ASPL's ability to induce condensates enriched in SG proteins depends on the presence of G3BP. We observed droplets upon the addition of 10 μM ASPL to lysates prepared from both G3BP-GFP–expressing cells and *G3BP1/2* DKO cells (fig. S2K). Therefore, we used LC-MS/MS to analyze the proteins in condensates formed by ASPL in each of these lysates and compared them to those in unseeded lysates. We identified 70 proteins uniquely enriched in ASPL-induced droplets isolated from G3BP-GFP–expressing lysates and 78 proteins from *G3BP1/2* DKO lysates, with 291 proteins similarly identified in both lysates (Fig. 2G and table S1D). GO analysis showed that proteins identified exclusively in ASPL-induced droplets from G3BP-GFP–expressing lysates were significantly enriched for factors involved in SG assembly [false discovery rate (FDR) = 3.24×10^{-7}]. In contrast, proteins found in ASPL-induced droplets from both G3BP-GFP–expressing and G3BP1/2 DKO lysates were predominantly enriched for factors involved in translation (Fig. 2H and table S1E). The enrichment of SG proteins in ASPL-induced droplets prepared from G3BP-GFP–expressing lysates but not from *G3BP1/2* DKO lysates suggests that ASPL's ability to promote condensates enriched in SG constituents depends on G3BP.

As ASPL's ability to induce SG-like condensates in lysates relied on the presence of G3BP, we sought to determine whether ASPL influences G3BP's ability to nucleate the formation of condensates. To test this hypothesis, we prepared lysates from U2OS cells stably expressing G3BP-GFP treated with either siCtrl or si*ASPL*. Increasing concentrations of purified G3BP were added to the lysates, and droplet formation was monitored using microscopy. Although G3BP+ droplets were observed in cell lysates derived from Ctrl cells and *ASPL*-depleted cells after the addition of recombinant G3BP (Fig. 2I), the total area occupied by the droplets (a product of their number and size) was reduced in *ASPL*-depleted lysates (Fig. 2J and fig. S2, L and M). Together, these findings suggest a direct relationship between the ASPL level and the probability of G3BP condensation, an indicator of the SG condensation threshold, in cells and lysates, with depletion of ASPL resulting in less condensation and higher levels of ASPL promoting condensation.

ASPL stabilizes G3BP interactions to lower the condensation threshold for SG formation

The SG condensation threshold is heavily influenced by the heterotypic interactions of G3BP with other SG constituents (*14*–*16*). Therefore, we used a semiquantitative LC-MS/MS approach to analyzing proteins that coimmunoprecipitated with G3BP and determined whether ASPL influences the G3BP interactome. To that end, we transfected *G3BP1/2* DKO human embryonic kidney (HEK) 293T cells with GFP-G3BP and treated them with either siCtrl or si*ASPL* before subjecting them to HS. As expected, the G3BP interactome from siCtrl cells showed a substantial overlap with established SG

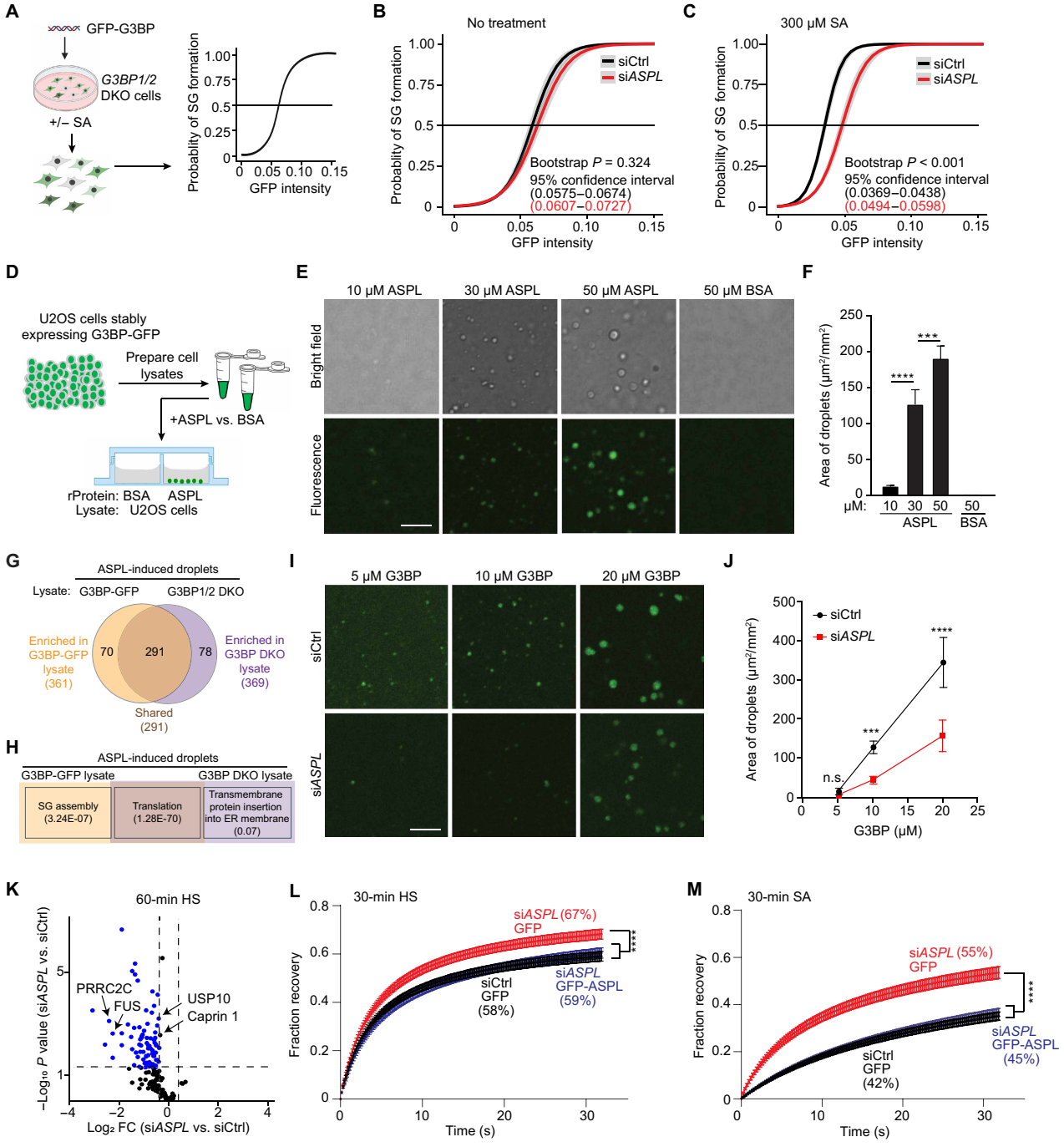

Fig. 2. ASPL regulates G3BP SG assembly in cell culture and in cell lysate. (**A**) Measuring threshold concentration of G3BP required for SG formation. Intensity of green is proportional to GFP-G3BP fluorescence. (**B** and **C**) si*ASPL* increases the threshold concentration for SG formation in U2OS cells upon 300 µM SA treatment (C), but not without treatment (B). The threshold concentration is defined as the G3BP concentration corresponding to 50% probability of SG formation. (**D** and **E**) Lysate granules from U2OS cells stably expressing G3BP-GFP via addition of purified recombinant ASPL or bovine serum albumin (BSA)–negative control. (**F**) Area of droplets as shown in (E). $n = 3$ images per condition. $^{***}P \leq 0.001$ and $^{****}P \leq 0.0001$ by ANOVA with Tukey's test. (**G**) Comparison of proteins enriched in ASPL-induced droplets from G3BP-GFP–expressing or *G3BP1/2* DKO cell lysates by mass spectrometry (MS). (**H**) Gene ontology (GO) analysis of proteins most highly enriched in ASPL-induced droplets from G3BP-GFP–expressing lysates compared to *G3BP1/2* DKO lysates. The top functional category for each group is shown with corresponding false discovery rate (FDR). ER, endoplasmic reticulum. (**I**) Addition of purified G3BP to G3BP-GFP U2OS cell lysates with siCtrl or si*ASPL*. (**J**) Droplet area in total imaging area as in (I). $n = 3$ images per condition. n.s., not significant; $^{***}P \leq 0.001$ and $^{****}P \leq 0.0001$ by ANOVA with Sidak's test. (**K**) Changes in spectral count of proteins identified in G3BP interactome after 60-min HS treatment at 43°C. Blue indicates proteins with significant decrease in G3BP interactome with si*ASPL*; vertical dashed line indicates 1.3-fold changes (FCs) in spectral count; horizontal dashed line indicates $P = 0.05$. PRRC2C, proline rich coiled-coil 2C; FUS, fused in sarcoma. $n = 4$ biological replicates. (**L** and **M**) FRAP of G3BP-tdTomato knock-in U2OS cells stably expressing GFP or GFP-ASPL and siCtrl or si*ASPL* after HS (L) or SA (M) treatment. $n = 15$ SGs (one SG/cell) per condition. Numbers in parentheses indicate mobile fraction of G3BP-tdTomato. $^{****}P \leq 0.0001$ by ANOVA with Tukey's test. Scale bars, 10 µm. Data are presented as means ± SEM.

proteins (https://rnagranuledb.lunenfeld.ca) (fig. S3A and table S1F). In siCtrl cells, we also detected the expected HS-induced increases in the number of interactions between G3BP and several SG-localized proteins that promote SG assembly, such as caprin 1 (fig. S3, B and C) (*58*). The expected increase in the G3BP-VCP interaction was also observed (fig. S3, B and C, and table S1G) (*4*). As indicated by the LC-MS/MS analysis and confirmed by immunoprecipitation-immunoblot analyses, many of these stress-induced changes were not observed in *ASPL*-depleted cells treated with HS or SA (fig. S3, D to F, and table S1G). Approximately one-third of G3BP binding partners had reduced interaction with G3BP upon *ASPL* depletion in HS-treated cells (Fig. 2K and fig. S3G), with minimal differences observed under baseline conditions (fig. S3H and table S1G). Proteins whose interactions with G3BP were reduced by depletion of *ASPL* in HS-treated cells were enriched with ribosomal proteins ($P < 0.0001$), helicases ($P < 0.0001$), Tric/CCT components ($P < 0.0001$), and other RNA binding proteins ($P < 0.0001$) (fig. S3G and table S1G).

Last, reasoning that a change in G3BP's interactions with other SG components might alter the material properties of G3BP+ SGs and influence G3BP mobility, we assessed ASPL's effect on this process with fluorescence recovery after photobleaching (FRAP) assays in G3BP-tdTomato knock-in U2OS cells. The mobile fraction of G3BP in similarly sized G3BP-tdTomato+ SGs increased upon RNAi-mediated depletion of endogenous *ASPL* in cells treated with HS or SA, but not in those stably expressing an RNAi-resistant form of *ASPL* (Fig. 2, L and M). Together, the results of the proteomics and FRAP analyses suggest that ASPL stabilizes G3BP's interaction with other SG components in response to stress, which could, in turn, lower the condensation threshold required for SG assembly.

ASPL promotes condensation of recombinant G3BP via its C-terminal UBX+ region

ASPL contains two ubiquitin-like (UBL) domains, a UBX domain, and two intrinsically disordered regions with nonuniform charge distributions as shown previously (*52*) and predicted by AlphaFold (*60*) (Fig. 3A and fig. S4A). The extended UBX region (UBX+; amino acids 377 to 553) encompasses the UBX and C-terminal intrinsically disordered regions. Because we observed a direct relationship between ASPL level and the probability of G3BP condensation in cells and lysates, we used a reductionist system that allows direct assessment of condensation behavior of purified proteins in vitro to determine whether ASPL is recruited to G3BP condensates and/or influences the LLPS behavior of G3BP. We generated a series of bacterial expression constructs and used them to purify recombinant full-length ASPL ("WT") and rationally designed deletion mutants, lacking either the first UBL domain (ΔUBL) or the UBX+ region (ΔUBX+) or containing only the UBX+ region (Fig. 3B).

Recombinant WT ASPL alone phase-separated under physiological salt concentrations (150 mM NaCl), in the presence of RNA (50 ng/ml) or in the presence of 10% Ficoll; however, this process required high concentrations (i.e., ≥100 μM ASPL) (fig. S4, B to E). Once formed, droplets composed of fluorescently labeled recombinant ASPL were dynamic and exhibited liquid-like properties (fig. S4F). We observed diminished LLPS with ΔUBX+; in contrast, droplets with UBX+ formed at lower concentrations than they did with WT ASPL (fig. S4G), suggesting that the phase separation potential of ASPL is restricted by intramolecular interactions.

After establishing baseline parameters for ASPL LLPS, we next assessed the ability of ASPL to be recruited into G3BP+ droplets. Fluorescently tagged ΔUBX+ showed less localization within G3BP+ droplets than did WT ASPL, whereas UBX+ was recruited more efficiently than WT ASPL (Fig. 3, C and D). Given the recruitment of ASPL into G3BP$^+$ droplets in vitro, we next tested whether ASPL and G3BP interact directly. Using recombinant WT ASPL, ΔUBL, or ΔUBX+ with glutathione *S*-transferase (GST)–tagged full-length G3BP in GST pull-down assays, we found a weak interaction between ASPL and G3BP that was mediated by the UBX+ region (Fig. 3, E and F).

We next sought to determine whether ASPL influenced the LLPS behavior of G3BP. When combined, WT ASPL and G3BP underwent LLPS at lower concentrations than either protein alone in the presence of RNA or Ficoll (Fig. 3, G to I, and fig. S4H). Although ΔUBL enhanced G3BP condensation in a manner similar to WT ASPL, ΔUBX+ failed to do so. Combining UBX+ with full-length G3BP also promoted the formation of droplets at lower concentrations than either protein alone (Fig. 3, G to I, and fig. S4H). Considering the critical role of the UBX+ domain in promoting G3BP condensation and enhancing the formation of SG-like assemblies, it was expected that recombinant ΔUBX+ showed an impaired ability to seed G3BP condensation in lysates (fig. S4, I and J).

C-terminal UBX+ region of ASPL alters the material properties of G3BP condensates

At higher concentrations of UBX+ (or with greater incubation times at lower concentrations), we observed that the droplets were somewhat irregular in shape and, upon closer examination, seemed to be formed by the clustering of smaller droplets (fig. S5A). Given this irregular morphology, we used thioflavin T (ThT) as a fluorescence probe and found unexpectedly that droplets prepared from full-length ASPL and UBX+ (but not ΔUBX+) were ThT+ (fig. S5B). This suggests either that the conformation of the UBX+ region in droplets includes β sheet–rich structures or that the droplets have a high macromolecular packing density (*61*, *62*). Droplets with a high packing density tend to show arrested fusion (*61*), which may help to explain the clustering of small droplets observed with high concentrations of UBX+. We also observed that, unlike droplets composed of G3BP alone (which were negative for ThT), those generated by mixing G3BP with WT ASPL (but not ΔUBX+) showed enhanced ThT fluorescence (fig. S5C), raising the possibility that ASPL alters the material properties of condensates.

To quantify the effects of ASPL and the UBX+ region on material properties of condensates formed by G3BP, we used viscoelastic particle tracking (VPT) nanorheology (*63*, *64*). The ensemble-averaged mean square displacement (MSD) profiles obtained from VPT using 200-nm fluorescently labeled probe particles revealed distinct differences in the viscoelastic properties of phase-separated condensates formed upon mixing G3BP with WT ASPL, ΔUBX+, and UBX+. First, we noted that the viscosity of condensates containing G3BP alone was higher than those formed from combining G3BP with ASPL (Fig. 3, J and K), suggesting that ASPL fluidizes G3BP droplets by introducing heterotypic buffering to the homotypic G3BP interaction network (*65*), resulting in a more fluid-like microenvironment within the condensate. G3BP condensates with UBX+ exhibited increased viscosity compared to those with full-length ASPL, whereas those containing ΔUBX+ displayed decreased viscosity (Fig. 3, J and K).

In addition to VPT, we calculated the partition coefficients of ASPL and G3BP in the condensates to quantify the extent of protein

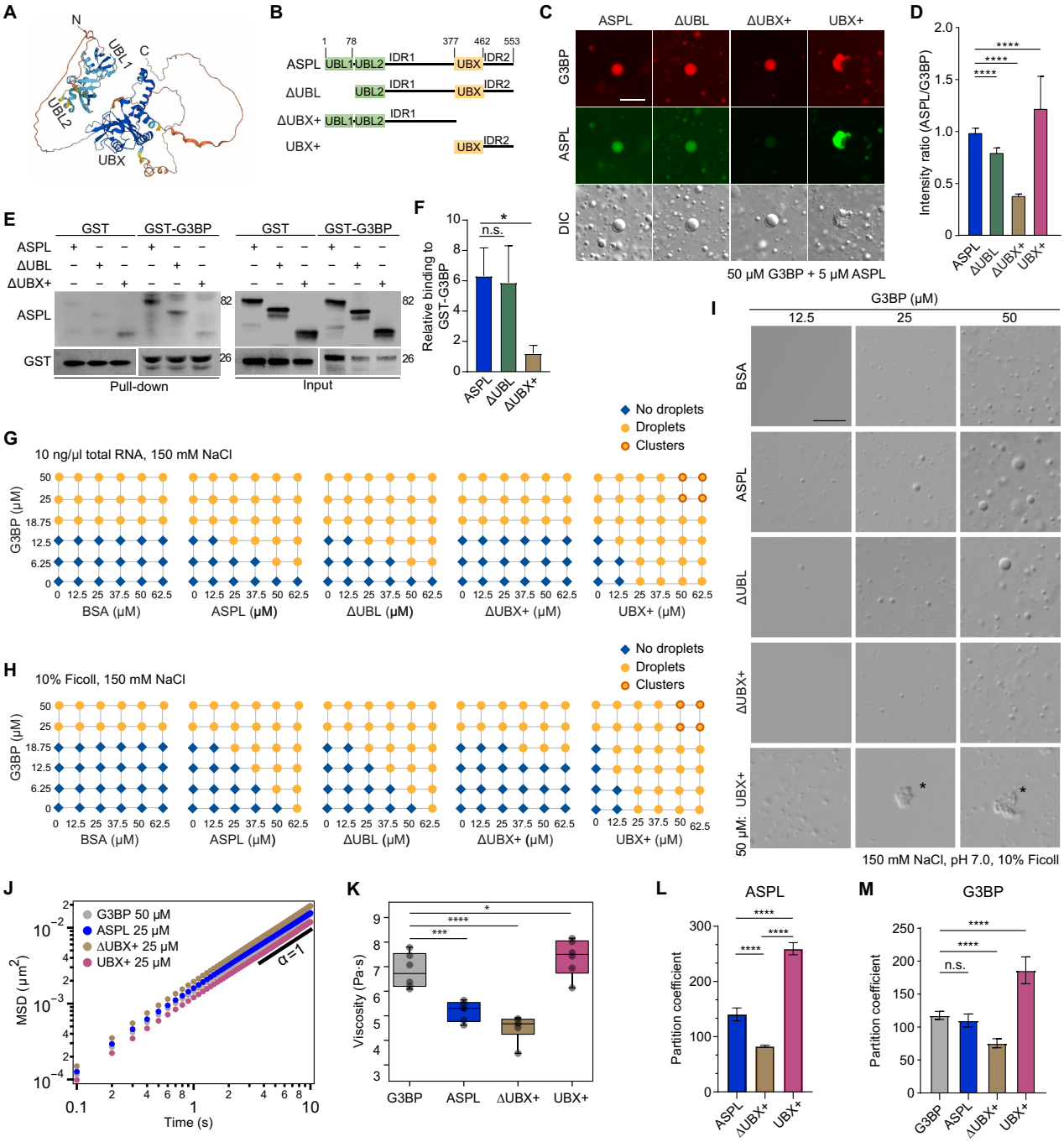

Fig. 3. ASPL promotes G3BP phase separation via its C-terminal extended UBX domain. (**A**) ASPL structure as predicted by AlphaFold. (**B**) Constructs used to investigate the function of ASPL domains. IDR, intrinsically disordered region. (**C** and **D**) Representative droplets formed by mixing Alexa Fluor 488 (AF488)–labeled recombinant ASPL (5 μM) and AF594–labeled G3BP (50 μM) (C). Fluorescence intensity of ASPL recombinant variants normalized to G3BP intensity (D). $n \geq 350$ droplets. $^{****}P \leq 0.0001$ by ANOVA with Tukey's test. (**E** and **F**) Pull-down of purified GST and GST-G3BP with purified ASPL proteins: full-length ASPL (WT), deletion of UBL (ΔUBL), and deletion of UBX+ (ΔUBX+) (E). Binding of ASPL variants by GST-G3BP normalized to pull-down by GST alone. $n = 3$. $^{*}P \leq 0.05$ by ANOVA with Tukey's test. (**G** and **H**) Phase separation behavior of purified ASPL variants with G3BP in 150 mM NaCl and total RNA (10 ng/μl) (G) or 150 mM NaCl and 10% Ficoll (H). (**I**) LLPS of 50 μM purified ASPL variant proteins versus BSA mixed with increasing amounts of G3BP in 150 mM NaCl and 10% Ficoll. (**J**) Ensemble-averaged mean square displacements (MSDs) determined from video particle tracking of 100 to 200 beads within condensates composed of G3BP and ASPL variants. Shift in MSDs from top to bottom signifies decreasing condensate mobility. (**K**) Viscosities estimated from fitting longer lag time ensemble-averaged MSDs to $\mathrm{MSD}(\tau) = 4D\tau^{\alpha} + N$. $n = 6$ condensates across two independent samples. Error bars are defined using median ± 1.5× interquartile range. $^{*}P \leq 0.05$, $^{***}P \leq 0.001$, and $^{****}P \leq 0.0001$ by Student's t test. (**L** and **M**) Partitioning of AF555–labeled ASPL variants (L) and AF488–labeled G3BP (M) was calculated as ratio of intensity values within condensates divided by average background intensity from five randomly chosen background regions. $n = 10$ condensates per technical replicate ($n = 3$). $^{****}P \leq 0.0001$ by ANOVA with Tukey's test. Scale bars, 20 μm. Data are presented as means ± SEM.

enrichment within the phase-separated droplets. The partition coefficient is calculated as the ratio of the concentration of ASPL or G3BP within the condensates to its concentration in the surrounding solution. Partition coefficients report on the transfer free energy of a macromolecule from the dilute phase to the dense phase, which is determined by intermolecular interactions between the condensate-forming components (*66*). The partition coefficients for both ASPL and G3BP were highest for UBX+, followed by WT ASPL, and lowest for ΔUBX+ (Fig. 3, L and M, and tables S1, H and I), consistent with the UBX+ region of ASPL mediating its interaction with G3BP. These values indicate that UBX+ promotes greater enrichment of ASPL and G3BP within the condensates, likely contributing to the observed increase in viscosity by facilitating more stable interactions. Conversely, the lower partition coefficient for ΔUBX+ suggests reduced enrichment and more fluid-like, dynamic condensates.

We also calculated the mobile fraction of each component in the condensates formed by mixing G3BP with ASPL (WT, UBX+, or ΔUBX+) using FRAP analysis. In contrast to nanorheology, which characterizes the time-dependent viscoelasticity of condensates by tracking the thermal motion of 200-nm beads, FRAP measures the recovery kinetics of fluorescently labeled proteins within a larger bleached region (>400 nm), reflecting not only viscous resistance but also the effects of biomolecular interactions in the dense phase and network viscoelasticity (*67*). We observed that the mobility of G3BP was increased in condensates formed in the presence of ΔUBX+ compared to WT ASPL and was slightly reduced in those formed by mixing G3BP with the UBX+ region alone (fig. S5D). Similarly, the mobile fractions of WT ASPL and UBX+ in G3BP+ condensates were comparable to each other and decreased relative to ΔUBX+ (fig. S5E). These results highlight the importance of the UBX+ domain when engaging in stable heterotypic interactions with G3BP, as this domain restricts the mobility of G3BP in condensates. The mobility of G3BP was higher in condensates containing ASPL than those formed from G3BP alone, consistent with the results of the VPT experiments.

Together, these results suggest that ASPL's UBX+ domain, which mediates its interaction with G3BP, alters the material properties of G3BP droplets and increases bulk condensate viscosity. The relative fluidization of G3BP condensates and increased mobility of G3BP upon addition of ASPL in vitro contrasts with the increased mobile fraction of G3BP observed in cells upon *ASPL* knockdown, highlighting the complex regulatory mechanisms governing G3BP condensation and mobility in different contexts. The endogenous G3BP:ASPL molar ratio in whole cell lysates ranges from 34:1 to 50:1 (fig. S5F); in contrast, a 2:1 ratio was used in our in vitro studies. This lower ratio more closely reflects the conditions present in cells overexpressing ASPL, as observed in our transfection experiments (Fig. 1B and fig. S1E), where ~50% of cells were transfected and ASPL-induced SGs were observed in cells expressing higher levels of ASPL. Thus, while the in vitro stoichiometry does not match endogenous levels, it is representative of cellular contexts in which ASPL is functionally active and capable of inducing SG formation.

ASPL's UBX+ region facilitates SG assembly

The results of our in vitro LLPS studies prompted us to investigate the importance of ASPL's UBX+ region in SG assembly. We generated a series of mammalian expression vectors containing full-length ASPL (WT) and deletion mutants (analogous to those used to produce recombinant proteins) fused in-frame to GFP; upon confirming their expression, we assessed their ability to promote the formation of spontaneous SG-like assemblies after transient overexpression. Whereas UBX+ showed an enhanced ability to promote the spontaneous formation of SG-like assemblies compared to ΔUBL and WT ASPL, ΔUBX+'s ability was impaired (Fig. 4, A and B, and fig. S6A). As expected, the UBX+ and ΔUBX+ mutants failed to interact with VCP (fig. S6B). We next used lentiviral vectors to stably express RNAi-resistant GFP-tagged WT ASPL or truncation mutants in G3BP-tdTomato knock-in U2OS cells and used live-cell imaging to assess SG formation in response to HS. We found that the assembly defect caused by si*ASPL* was rescued by expression of RNAi-resistant WT ASPL and ΔUBL, but not by ΔUBX+ (Fig. 4, C and D; fig. S6, C to F; table S1A; and movie S2). We next examined the mobility of G3BP in SGs by FRAP after exposing these cells to HS or SA. Although expression of ΔUBL decreased the mobile fraction of G3BP similar to WT ASPL, expression of ΔUBX+ failed to do so, consistent with the UBX+ region mediating heterotypic interactions with G3BP and reducing the threshold for G3BP condensation (Fig. 4, E and F). These results suggest that the interaction between G3BP and ASPL's UBX+ region enhances G3BP condensation, alters the material properties of the SG condensate, and stabilizes the interaction of G3BP with other SG constituents, ultimately reducing the exchange rate between SG-localized G3BP with cytosolic G3BP and promoting SG formation.

ASPL forms a stable complex with VCP hexamers at physiological molar ratios

VCP-mediated extraction of G3BP helps maintain the dynamic liquid-like properties of SGs, facilitating their disassembly upon the removal of inciting stressors (*3*, *4*). Prior studies, confirmed by our own, have shown that when ASPL and VCP are combined at a 1:1 molar ratio in vitro or upon overexpression of ASPL in cells, ASPL's interaction with VCP promotes the disassembly of VCP hexamers and stabilizes VCP:ASPL heterotetramers (*52*) (fig. S1G). Given that the hexameric structure of VCP is essential for its function, our finding that ASPL's interaction with VCP is required for the efficient disassembly of SGs seemed to be at odds with these prior results. Therefore, we sought to investigate the nature of the interaction between ASPL and VCP hexamers under physiological conditions.

First, we examined the migration patterns of ASPL and VCP in 3×-FLAG–ASPL cells generated by CRISPR-Cas9–mediated knock-in using blue native gel electrophoresis, followed by immunoblot analyses (fig. S6G). We observed multiple bands using an anti-FLAG antibody, including one near the 720-kDa marker. The intensity of this band decreased upon RNAi-mediated knockdown of *VCP* (fig. S6, G and H), suggesting that its formation depended on VCP. We also detected a band near the 720-kDa marker using an anti-VCP antibody, presumably corresponding to intact hexamers, with or without additional proteins (fig. S6G). To more definitively identify complexes containing both ASPL and VCP, we immunoprecipitated endogenous ASPL from the 3×-FLAG–ASPL cells using anti-FLAG antibody. Immunoprecipitates were analyzed via blue native gel electrophoresis, followed by immunoblot analysis. Immunoblot analyses using anti-FLAG antibody revealed multiple bands ranging in size from ~146 to 720 kDa, indicating that ASPL is present in complexes of varying molecular sizes (Fig. 5A). Bands near the 720-kDa marker were detected using both anti-FLAG and anti-VCP antibodies. The intensity of these bands decreased upon RNAi-mediated knockdown of *VCP* (Fig. 5A). We did not detect VCP in lower–molecular weight

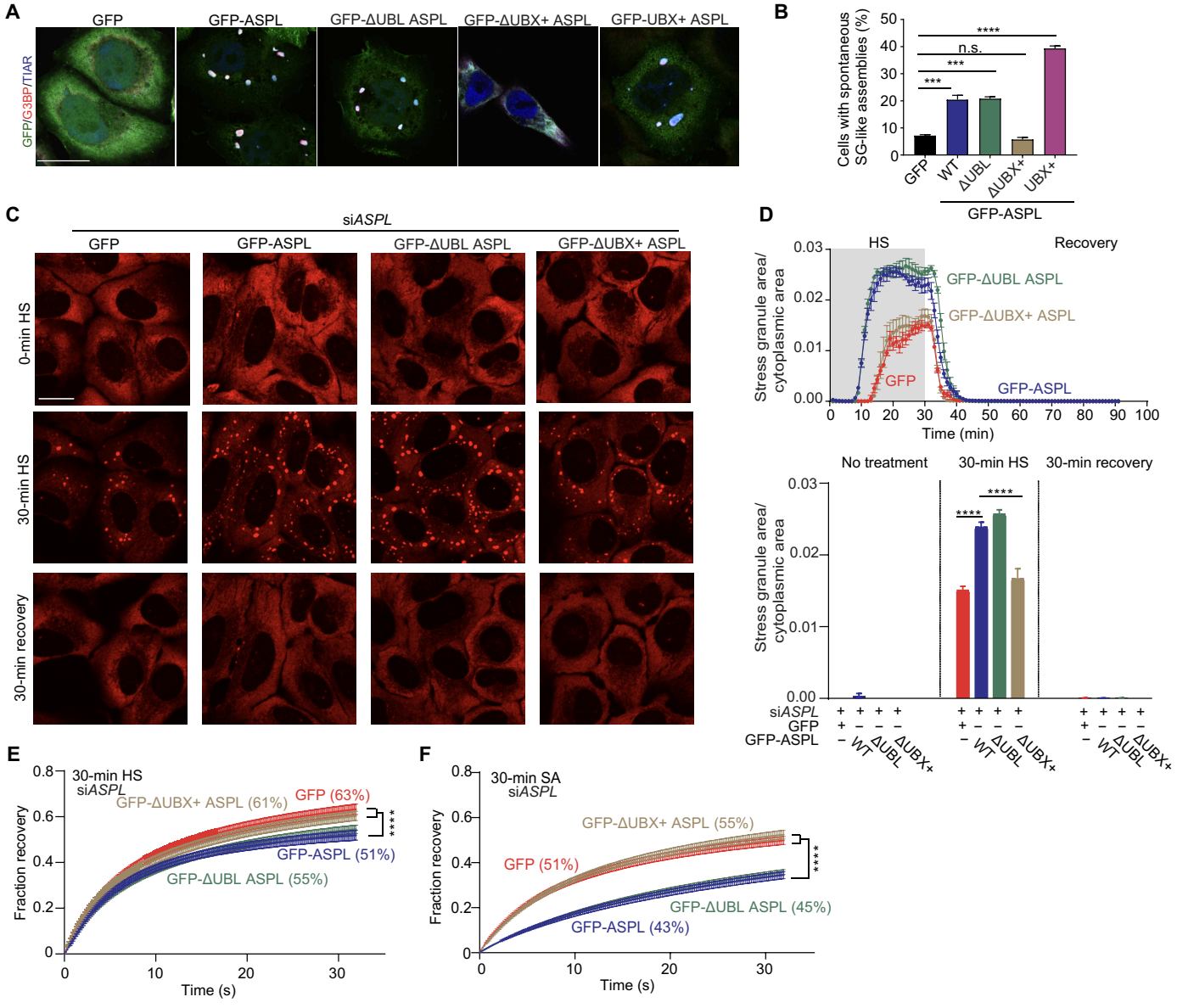

Fig. 4. The UBX+ domain of ASPL drives SG assembly in cells. (**A**) HeLa cells were transfected with indicated GFP or GFP-ASPL plasmids and stained to detect spontaneous SG-like assemblies. (**B**) Percentages of cells from (A) containing spontaneous SG-like assemblies. $n > 100$ cells from two biological replicates. $^{***}P \leq 0.001$ and $^{****}P \leq 0.0001$ by ANOVA with Tukey's test. (**C**) Live-cell imaging of G3BP-tdTomato knock-in U2OS cells stably expressing GFP, GFP-ASPL, GFP-ΔUBL ASPL, or GFP-ΔUBX+ ASPL, and siRNA against *ASPL*. Cells were subjected to 30-min HS treatment at 43°C, followed by 1-hour recovery at 37°C. (**D**) Area occupied by SGs was normalized to cytoplasmic area from cells as shown in (C). $n > 60$ cells from a representative experiment. $^{****}P \leq 0.0001$ by ANOVA with Tukey's test. (**E** and **F**) FRAP of SGs in G3BP-tdTomato knock-in U2OS cells stably expressing GFP, GFP-ASPL, GFP-ΔUBL ASPL, or GFP-ΔUBX+ ASPL, along with siRNA against *ASPL* after 30-min HS (E) or SA (F) treatment. $n \geq 15$ SGs for each treatment. $^{****}P \leq 0.0001$ by ANOVA with Tukey's test. Numbers in parentheses indicate mobile fraction of G3BP-tdTomato. Scale bars, 20 μm. Data are presented as means ± SEM.

complexes corresponding to the VCP-ASPL heterotetramers formed when the proteins are mixed at 1:1 molar ratios (*52*) in either the lysates or ASPL immunoprecipitates, suggesting that endogenous ASPL exists in a complex with intact VCP hexamers.

Next, we compared the molar ratio of endogenous ASPL and VCP in cell lysates and found that VCP levels were ~90-fold higher than ASPL levels under physiological conditions (fig. S6I). This difference in concentration underscores the importance of studying the ASPL-VCP interaction at relevant molar ratios in vitro. To evaluate the nature of the ASPL-VCP interaction, we used a combination of fluorescence-detected sedimentation velocity analytical ultracentrifugation (FDS-SV-AUC) and interference SV-AUC experiments with a 1:84 ratio of ASPL to VCP monomers [0.2 μM Alexa Fluor 488 (AF488)–ASPL to 16.8 μM VCP] to approximate physiological conditions. FDS-SV-AUC was chosen for its sensitivity in detecting fluorescently labeled molecules, allowing us to specifically track ASPL in the presence of excess VCP. Interference SV-AUC was used to provide a comprehensive analysis of all protein species in the mixture,

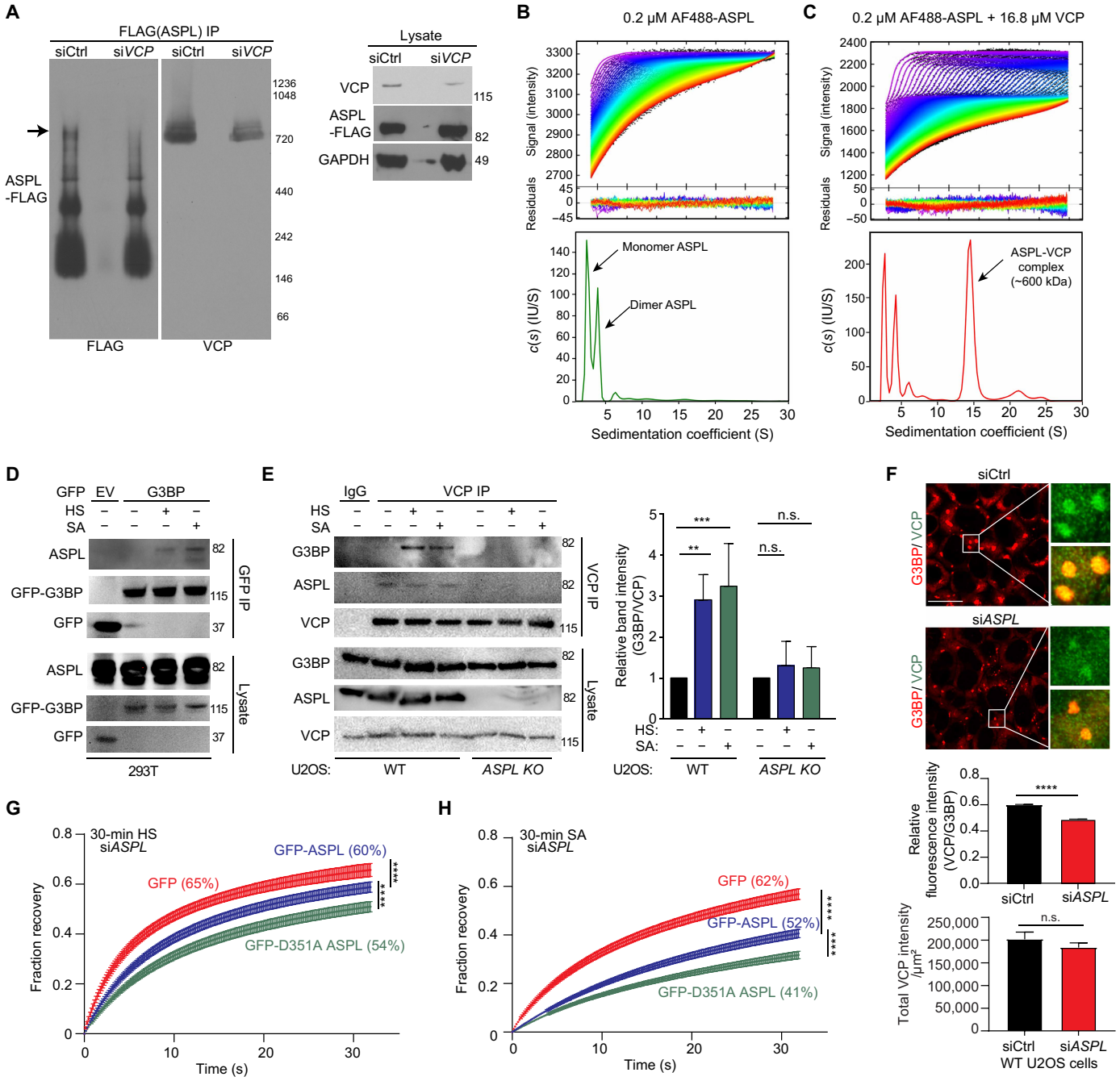

Fig. 5. ASPL promotes recruitment of VCP hexamer to G3BP granules. (**A**) HeLa cells with knock-in 3× C-terminal FLAG-tagged ASPL expressing nontargeting siCtrl or si*VCP* were subjected to coimmunoprecipitation (IP) using FLAG antibodies, followed by blue native polyacrylamide gel electrophoresis (PAGE) (left). Arrow indicates band corresponding to ASPL bound to a VCP hexamer. SDS-PAGE shows the inputs (right). GAPDH, glyceraldehyde-3-phosphate dehydrogenase. (**B** and **C**) FDS-SV-AUC data of 0.2 μM AF488-ASPL (B) and mixture of 0.2 μM AF488-ASPL with 16.8 μM VCP (C). Fluorescence intensity scans (top) are plotted against distance from axis of rotation. Data were subjected to standard *c*(*s*) analysis in SEDFIT (*101*, *102*) (solid lines, rainbow color scheme). Corresponding sedimentation coefficient distributions are shown below. (**D**) Coimmunoprecipitation of GFP-G3BP followed by immunoblotting for ASPL and GFP in HEK293T cells cotransfected with GFP-G3BP– and Myc-DDK–tagged ASPL after 60-min HS treatment at 43°C or 30-min 500 μM SA treatment. EV, empty vector. (**E**) Coimmunoprecipitation with VCP antibody in WT and *ASPL* KO U2OS cells after HS or SA treatment. $n = 3$. $^{**}P \leq 0.01$ and $^{***}P \leq 0.001$ by ANOVA with Sidak's multiple comparisons test. (**F**) HeLa cells transfected with siCtrl or si*ASPL* and stained after 60-min HS treatment. Scale bar, 20 μm. Relative fluorescence intensity (VCP/G3BP) (top) and total VCP intensity per square micrometer (bottom). $n \geq 200$ granules from two biological replicates. $^{****}P < 0.0001$ by Student's *t* test. (**G** and **H**) FRAP of SGs in G3BP-tdTomato knock-in U2OS cells stably expressing GFP, si*ASPL*-resistant GFP-ASPL, or GFP-D351A ASPL, along with siRNA against *ASPL* subjected to 30-min HS (G) or SA (H) treatment. $n = 15$ SGs (one SG/cell) per condition and two biological replicates. For (G) and (H), numbers in parentheses indicate mobile fraction of G3BP-tdTomato. $^{****}P \leq 0.0001$ by ANOVA with Tukey's test. Data are presented as means ± SEM.

regardless of labeling, ensuring accurate measurement of VCP and its complexes.

When analyzed alone, AF488-labeled ASPL (AF488-ASPL) displayed two predominant species corresponding to monomeric and dimeric forms (Fig. 5B). Upon mixing with VCP, the FDS-SV-AUC revealed a notable peak at 14.56 S with a molecular weight approximating the theoretical mass of a VCP hexamer bound to an ASPL monomer (599,698 Da), indicating complex formation (Fig. 5C and table S1J). This was further corroborated by the two-dimensional size-and-shape distribution analysis, which confirmed the presence of a major species with a sedimentation coefficient of 14.44 S and a molecular weight of 594,438 Da, consistent with an ASPL-VCP hexamer complex (fig. S6J and table S1K).

In contrast, the interference SV-AUC analysis showed a dominant peak at 14.13 S, corresponding to the VCP hexamer, reflecting its excess concentration in the mixture (fig. S6, K to N, and table S1L). The height of this dominant VCP peak in the interference data was much higher than the corresponding peak in the fluorescence data. The difference in peak size between the fluorescence and interference data indicates that while VCP predominantly remains in its hexameric form due to its high concentration, the fluorescence data specifically highlight the ASPL-VCP hexamer complex. Together, the results of the SV-AUC analyses suggest that ASPL binds to VCP in a 1:6 ratio, forming a stable complex. The chosen molar ratios for the SV-AUC experiments were crucial in elucidating these interactions and facilitated the detection of the ASPL-VCP hexamer complex, corroborating the results of the ASPL immunoprecipitation analyses.

ASPL is required for efficient VCP-mediated extraction of G3BP from SGs

Our studies demonstrating interactions between ASPL and VCP hexamers and between recombinant ASPL and G3BP, combined with our unbiased proteomics data suggesting that ASPL stabilizes the G3BP-VCP interaction in stressed cells, led us to hypothesize that ASPL helps catalyze the extraction of G3BP by VCP. To test this hypothesis, we first performed immunoprecipitation assays to determine whether the ASPL-G3BP interaction could be detected in cell lysates. We detected an interaction between ASPL and GFP-G3BP but only after subjecting cells to HS or SA (Fig. 5D). Using both WT and *ASPL* KO cells, we found that the stress-induced interaction between endogenous VCP and G3BP was absent in cells lacking ASPL (Fig. 5E). We next assessed the levels of VCP recruited to G3BP+ SGs within cells after RNAi-mediated knockdown of *ASPL*. We observed a small but significant ($P < 0.0001$) decrease in the level of VCP localizing to SGs in si*ASPL* cells compared to siCtrl cells, while the total levels of VCP remained unchanged (Fig. 5F). These observations suggest that although ASPL may be one of many factors contributing to the recruitment of VCP to SGs, it is a key factor in recruiting VCP to G3BP.

To assess ASPL's role in facilitating the VCP-mediated exchange of SG-localized G3BP with its cytoplasmic pools in stressed cells, we performed FRAP assays in si*ASPL* cells stably expressing G3BP-tdTomato and either WT ASPL or the VCP binding–defective ASPL D351A mutant. We found that expression of the D351A mutant in cells treated with HS (Fig. 5G) or SA (Fig. 5H) resulted in a reduction in the mobile fraction of G3BP compared to that in cells expressing WT ASPL. This result was similar to the reduction in the mobile fraction of G3BP observed in cells treated with the VCP inhibitor CB-5083 in stressed cells (fig. S6, O and P).

ASPL is required for ULK-mediated phosphorylation and activation of VCP

We previously demonstrated that the serine-threonine kinases ULK1 and ULK2, independent of their roles in autophagy, play a key role in the efficient disassembly of SGs by phosphorylating VCP at serine-13, serine-282, and threonine-761 (*3*). Moreover, the conditional disruption of *Ulk1/2* expression in skeletal muscle causes a vacuolar myopathy with SQSTM1+, ubiquitin+, and TDP43+ inclusions in mice (*3*), similar to that caused by the expression of pathogenic VCP mutations (*3*, *33*, *35*, *68*, *69*). Notably, using an unbiased proteomics approach, we previously found the presence of ASPL (in addition to VCP) within the ULK1 interactome (*3*). To follow up on this observation, we immunoprecipitated overexpressed or endogenous ASPL and performed immunoblot analyses to define the relationship among ULK1/2, VCP, and ASPL. We found that interactions between ASPL and ULK1 or ULK2 were stabilized in the presence of either HS-induced (fig. S7, A and B) or SA-induced stress (Fig. 6A and fig. S7, C and D). In addition, we found that the ULK1-VCP interaction was reduced in stressed cells after knockdown or KO of *ASPL* (Fig. 6, B and C, and fig. S7E), whereas the ULK1-ASPL interaction was minimally affected by *VCP* knockdown (fig. S7E). To confirm the importance of ASPL in the stabilization of the ULK1-VCP interaction, we used a split luciferase-based NanoBiT (NanoLuc Binary Technology) assay (*70*), in which ULK1 was fused to the large BiT (LgBiT; 18 kDa) subunit of luciferase and VCP was fused to the small BiT (SmBiT). We used this system in *ASPL*-depleted HEK293T cells coexpressing ULK1-LgBiT and VCP-SmBiT. We observed an eightfold increase in luminescence of cells upon coexpression of ASPL-GFP (but not GFP alone) upon SA treatment (Fig. 6D), indicating that ASPL was required to mediate the ULK1-VCP interaction. We next tested the effect of expressing the ASPL mutants D351A and PPAA, which are defective in binding VCP but retain the ability to interact with ULK1 (fig. S7F), and found that these ASPL mutants did not support the stress-induced increase in luminescence (Fig. 6D), highlighting the importance of ASPL in bridging ULK1 and VCP.

We next sought to determine whether the ability of ASPL to stabilize the ULK1-VCP interaction also influenced the ability of ULK1 to phosphorylate VCP (*3*). We generated an antibody against phosphorylated serine-13 of VCP (pVCP) and confirmed that it detected ULK1/2-dependent VCP phosphorylation (fig. S7G). This antibody detected the stress-induced increase in VCP phosphorylation in WT U2OS cells treated with HS or SA but not in *ASPL* KO U2OS cells under similar conditions (Fig. 6, B and C). VCP phosphorylation was restored in si*ASPL* cells stably expressing WT ASPL but not the VCP binding–defective ASPL mutants (Fig. 6E). We also used the generated antibody to examine VCP phosphorylation in skeletal muscle collected from adult mice. The serine-13–phosphorylated VCP was detected in skeletal muscle from WT but not *Aspl* KO mice (Fig. 6F). These results indicate that the phosphorylation of VCP relies on the presence of ASPL in skeletal muscle and in cultured cells subjected to stress.

To assess the functional relevance of ASPL in ULK-mediated phosphorylation of VCP, we next performed live-cell imaging assays using G3BP-tdTomato knock-in U2OS cells stably expressing WT GFP-ASPL or D351A GFP-ASPL and either WT VCP or a phosphomimetic VCP mutant in which all three ULK-dependent phosphorylation sites (serine-13, serine-282, and threonine-761) were mutated to aspartates (3SD). Our previous study demonstrated that the 3SD VCP mutant rescues SG disassembly defects in cells depleted of both

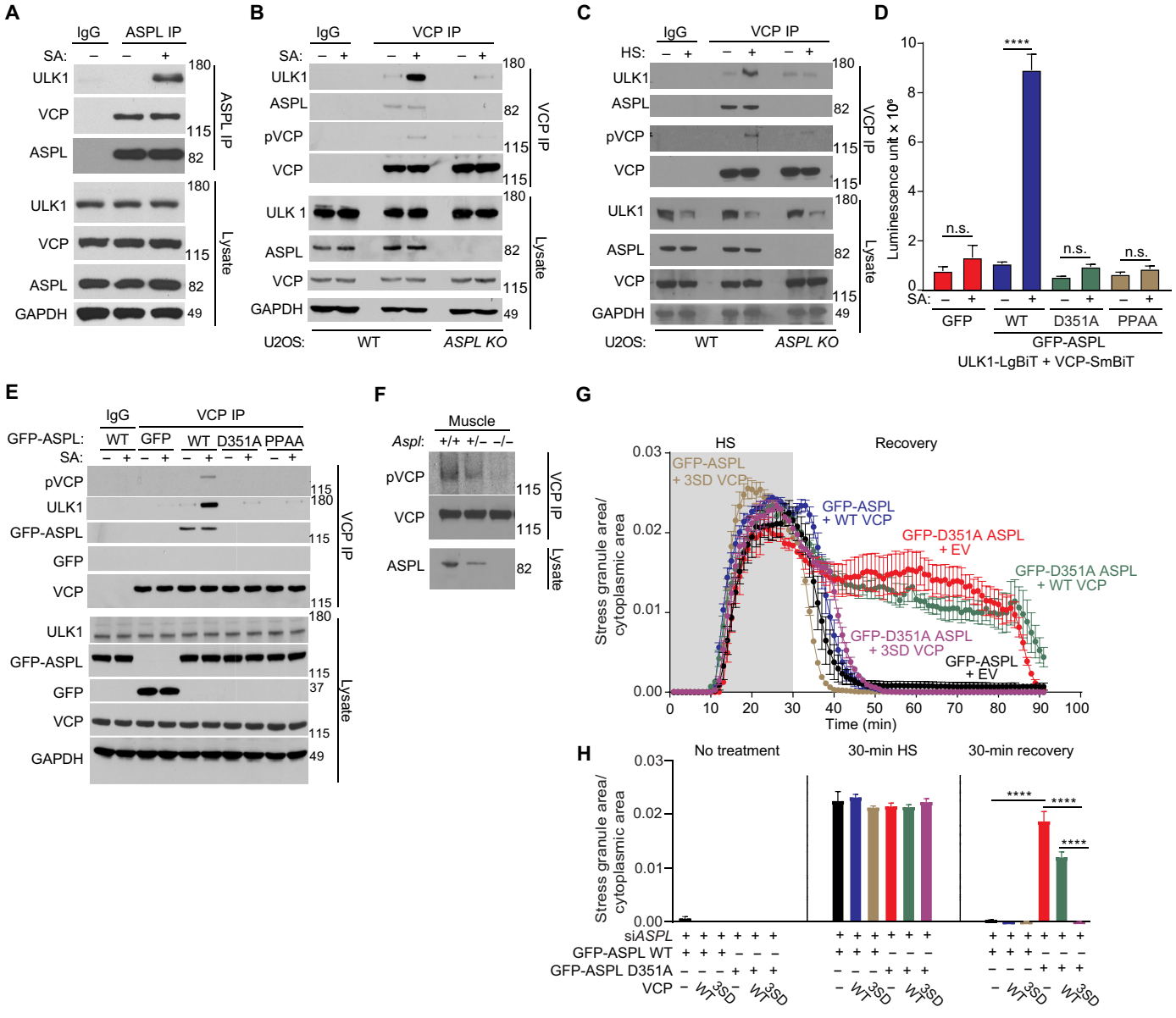

Fig. 6. ASPL mediates ULK-VCP interaction to facilitate VCP phosphorylation. (**A**) Representative immunoblots of endogenous ASPL immunoprecipitated from 3×-FLAG ULK1 mouse embryonic fibroblasts (MEFs) subjected to 60-min 500 μM SA treatment. (**B** and **C**) WT and *ASPL* KO U2OS cell lines were transfected with VCP plasmid and treated with SA (B) or 60-min HS at 43°C (C), followed by immunoprecipitation using VCP antibody. (**D**) HEK293T cells were transfected with indicated plasmids and siRNA against *ASPL*. GFP-ASPL constructs are si*ASPL*-resistant. Cells were subjected to 30-min SA treatment, and luminescence signal was measured. ****$P \leq 0.0001$ by ANOVA with Sidak's multiple comparisons test. (**E**) U2OS cell lines stably expressing indicated ASPL variants were transfected with VCP plasmid and siRNA against *ASPL*. Cells were subjected to SA treatment, followed by immunoprecipitation using VCP antibody. (**F**) Representative immunoblots of endogenous VCP immunoprecipitated from WT *Aspl* (+/+), heterozygous *Aspl* (+/−), and homozygous *Aspl* (−/−) mouse skeletal muscle tissues. (**G**) Area occupied by SGs divided by cytoplasmic area from live-cell imaging of G3BP-tdTomato knock-in U2OS cells stably expressing indicated genes. GFP-ASPL constructs are si*ASPL*-resistant. Cells were transfected with siRNA against *ASPL* and subjected to 30-min HS treatment, followed by recovery at 37°C. $n > 60$ cells from representative experiment. (**H**) Area occupied by SGs divided by cytoplasmic area (G) before HS treatment, after 30 min of HS treatment, and after 30 min of recovery. ****$P \leq 0.0001$ by ANOVA with Tukey's test. Data are presented as means ± SEM.

VCP and ULK1, whereas WT VCP is unable to do so (*3*). As described above, SG disassembly was delayed in cells expressing the D351A ASPL mutant. The aberrant disassembly process was rescued in cells expressing 3SD VCP but not in those expressing WT VCP (Fig. 6, G and H; fig. S7, H and I; table S1A; and movie S3). This result is consistent with our hypothesis that ASPL facilitates ULK-mediated phosphorylation of VCP, which is required for efficient SG disassembly.

SG disassembly defect associated with pathogenic VCP mutations can be rescued by mimicking ULK-mediated phosphorylation or *ASPL* knockdown

Mutations affecting the R155 position of VCP account for almost 50% of cases of MSP (*41*, *71*). These mutations affect the nucleotide-driven allosteric regulation of VCP and, more specifically, the coupling between the D1 and N-terminal domains of VCP (*72*). When

expressed in cultured cells, the most common MSP-causing VCP mutant, R155H, impairs the disassembly of HS-induced SGs (*4*). The R155H VCP mutant has also been hypothesized to have a reduced interaction with ASPL (*55*). To determine whether altered interaction between R155H VCP and ASPL contributes to the SG disassembly defect associated with R155H, we first examined its interactions with ASPL and ULK1 by coimmunoprecipitation. We found a reduction in interaction between R155H VCP and ASPL compared to that with WT VCP. This was accompanied by a reduction in the R155H VCP-ULK1 interaction and in VCP phosphorylation at serine-13 in cells treated with SA (Fig. 7A) or exposed to HS (Fig. 7B). We observed similar defects in the ASPL-VCP and ULK1-VCP interactions and in ULK-mediated phosphorylation of another N-terminal VCP mutant, R159H VCP, which also causes MSP (Fig. 7B) (*73*–*77*). On the basis of these results, we hypothesized that impaired ULK-mediated phosphorylation of certain VCP mutants (secondary to the weaker interaction with ASPL) contributes to the associated SG disassembly defect.

To test this hypothesis, we introduced phosphomimetic serine/threonine to aspartate substitutions at serine-13, serine-282, and threonine-761 of R155H (or R159H) VCP to bypass the need for ULK-mediated phosphorylation. The SG disassembly defects observed in cells expressing R155H or R159H were rescued in cells expressing R155H or R159H VCP with the phosphomimetic 3SD substitutions (Fig. 7, C to F; table S1A; and movies S4 and S5), highlighting the importance of the ability of ASPL to facilitate ULK-mediated VCP phosphorylation during SG disassembly.

Despite ASPL's role in enabling ULK-mediated phosphorylation of VCP and maintaining G3BP mobility, cells depleted of ASPL had impaired SG assembly only, with no observed defects in disassembly (Fig. 1F). Therefore, we considered the balance between ASPL's role in assembly, where ASPL stabilizes interactions between G3BP and other SG constituents, and ASPL's role in disassembly, where the ASPL-VCP interaction is required for the efficient extraction of G3BP from SGs. We hypothesized that decreasing levels of ASPL might alter SG dynamics such that the requirement of VCP for SG disassembly might also be affected. When ASPL was depleted from cells expressing R155H or R159H VCP, they not only showed defects in SG assembly but also no longer showed defects in SG disassembly (Fig. 7, G to J; table S1A; and movies S6 and S7). This suggests that SGs formed in the absence of ASPL do not rely on the ASPL-VCP interaction for disassembly, reinforcing the hypothesis that the ability of ASPL to induce SG formation in cells is counterbalanced by its ability to recruit and activate VCP for SG disassembly.

DISCUSSION

This study reveals a previously unknown function of ASPL in regulating RNP granule dynamics, specifically as a factor that couples the assembly and disassembly of SGs. We first demonstrated that ASPL, independent of its interaction with VCP, facilitates SG assembly. As the aberrant persistence of SGs and related RNP granule assemblies may contribute to the pathologic fibrillization of TDP43 (*26*, *30*, *32*, *78*–*81*), factors that lower the threshold for RNP granule assembly may pose a threat to cells if left unchecked. We found that ASPL's role in SG assembly is counterbalanced by stabilizing interactions between G3BP and VCP and promoting ULK-mediated phosphorylation of VCP, which helps maintain the mobility of G3BP and the dynamic fluid-like properties of SGs that are required for the disassembly of SGs upon the removal of the inciting stressors (*3*, *4*, *14*). Thus, by modulating various protein-protein interactions, ASPL links G3BP condensation with the disassembly activity of VCP.

The observation that ASPL enhances the interactions of G3BP with other SG components and promotes SG assembly fits well into the working model of RNP granule assembly via percolation-coupled phase transition (*65*, *82*, *83*). In this model, phase transition and SG assembly occur when the sum and duration of localized protein-protein interactions are sufficient to create a system-spanning network. We found that the interaction of ASPL with G3BP, via its UBX+ region, alters the material properties of droplets by restricting G3BP mobility and increasing viscosity within the condensates. In cells, this may strengthen the SG network of interactions, thereby reducing the SG condensation threshold and promoting SG assembly. These findings support a central role for G3BP in facilitating a percolation-like process in SG formation, where ASPL accelerates assembly by promoting critical interactions between G3BP and other SG components.

Although ASPL also stabilizes the G3BP-VCP interaction, it is not the sole cofactor that recruits VCP to SGs. For instance, ZFAND1 (zinc finger AN1-type containing 1) recruits VCP to SGs induced by SA and is critical for the disassembly of SGs induced by SA but not HS (*5*). In contrast, FAF2 (Fas-associated factor family member 2) interacts with ubiquitinated G3BP under HS treatment and is essential for SG disassembly following HS but not SA treatment (*4*). However, unlike ZFAND1 and FAF2, which function in a stress-specific manner, by stabilizing the G3BP-VCP and ULK1-VCP interactions, ASPL promotes ULK-mediated phosphorylation of VCP and SG disassembly under both conditions, thus providing a mechanism for the spatiotemporal regulation of VCP activity. Although the HS-induced ubiquitination of G3BP is required for its efficient extraction by VCP and the rapid disassembly of SGs upon restoration of normal temperature (*4*), ubiquitination of G3BP is less pronounced in SA-treated cells, and ubiquitination of G3BP or other SG proteins is not essential for the relatively slower disassembly of SGs formed in response to this stress (*4*, *84*, *85*). Although many VCP substrates are ubiquitinated, there are examples of VCP substrates that are not (*86*, *87*). Therefore, our observations of both the reduced mobility of G3BP in cells expressing the VCP binding–defective mutant and the ASPL-mediated stabilization of the G3BP-VCP interaction in cells subjected to either SA or HS suggest a role for the ASPL-VCP interaction in the VCP-mediated extraction of G3BP independent of G3BP's ubiquitination status. Future in vitro reconstitution and in vivo studies are required to determine the relationship(s) between the ubiquitination status of G3BP, different VCP cofactors, and their relative contributions to condensate and SG dynamics.

Our results provide the first evidence that endogenous ASPL can form a stable complex with VCP hexamers in cells and in vitro when present at physiological molar ratios. These findings illustrate how ASPL functions as a bridge between ULK1 and VCP. ASPL is also thought to promote VCP methylation by serving as a bridge between the methyltransferase METTL21D and VCP (*55*, *88*, *89*), but, in that case, the binding of ASPL is thought to promote structural remodeling of VCP hexamers, exposing lysine-315 to facilitate its trimethylation by METTL21D (*88*, *89*). Although certain disease-causing VCP mutants (R155H, R159G, and R191Q) are resistant to the methylation-promoting effects of ASPL, the physiologic consequences of this posttranslational modification (which reduces VCP activity) and how it relates to disease remain unclear (*55*).

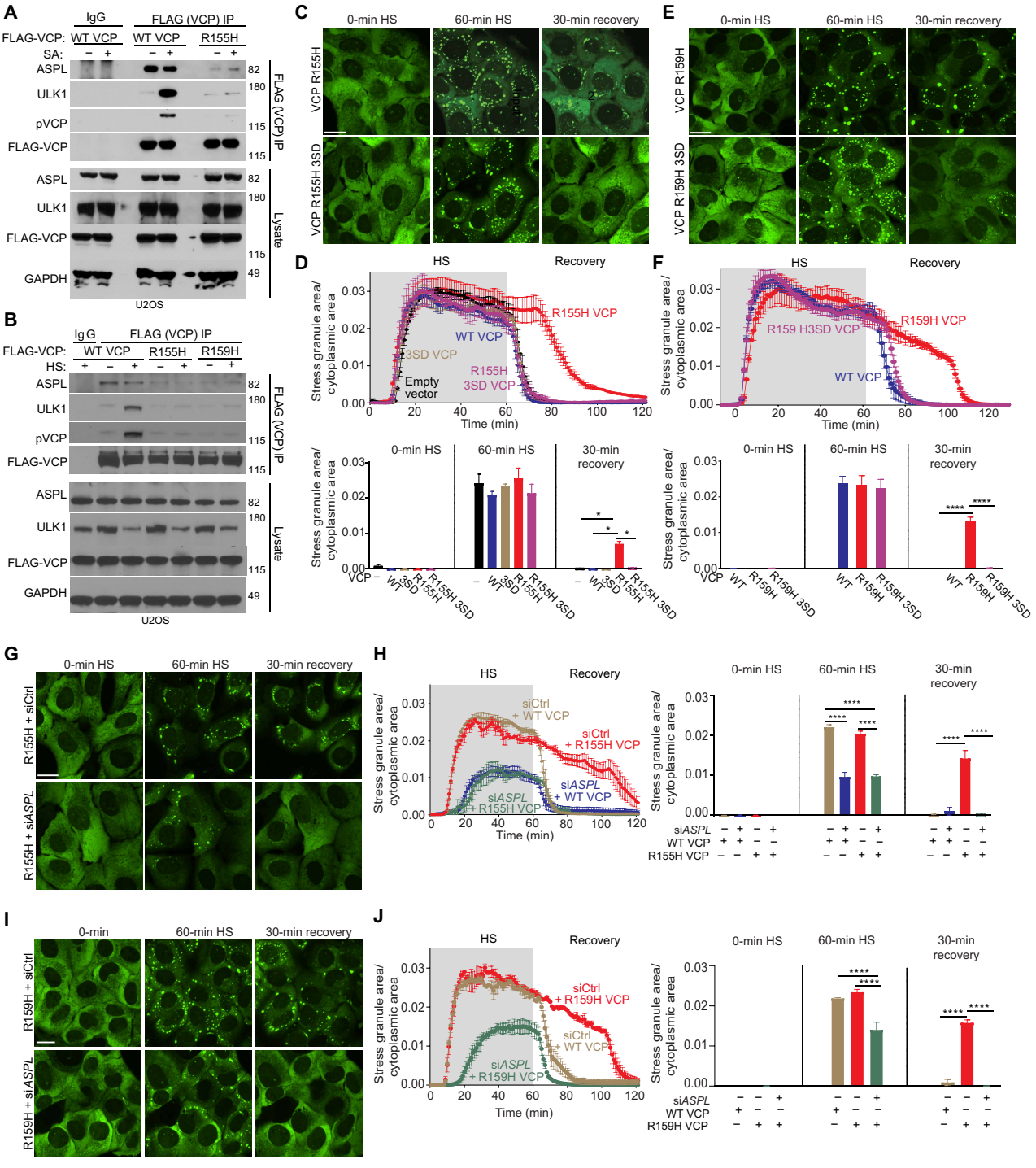

Fig. 7. Reduced VCP–ASPL interaction underlies SG disassembly defect associated with VCP mutants. (**A** and **B**) FLAG-tagged WT or mutant VCP variants were transfected into U2OS cells. After 48 hours, cells were treated with 500 μM SA for 60 min (A) or 60-min HS at 43°C (B). VCP was immunoprecipitated using FLAG antibody and immunoblotted. Mouse preimmune immunoglobulin G (IgG) was used as a control. (**C** to **F**) Live-cell imaging of U2OS cells stably expressing GFP-G3BP and indicated blue fluorescent protein (BFP)–tagged VCP R155H (C) and R159H (E) expressing plasmids. Area occupied by SGs normalized to cytoplasmic area in R155H (D) and in R159H (F) expressing cells after 60-min HS treatment, followed by recovery at 37°C. $n > 60$. Bar graph illustrates the area occupied by SGs normalized to cytoplasmic area in cells before HS treatment, after 60 min of HS treatment, and after 30 min of recovery. $^{*}P \leq 0.05$ and $^{****}P \leq 0.0001$ by ANOVA with Tukey's test. (**G** to **J**) Live-cell imaging of U2OS cells stably expressing GFP-G3BP and BFP-tagged VCP R155H (G) or R159H (I) was transfected with siCtrl or si*ASPL*. Area occupied by SGs normalized to cytoplasmic area in cells expressing R155H (H) and R159H (J) VCP variants after 60-min HS treatment, followed by 1-hour recovery at 37°C. $n > 60$ cells. Bar graph shows the area occupied by SGs normalized to cytoplasmic area in cells before HS treatment, after 60 min of HS treatment, and after 30 min of recovery. $^{****}P \leq 0.0001$ by ANOVA with Tukey's test. Scale bars, 20 μm. Data are presented as means ± SEM.

In contrast, a role for ASPL in enabling ULK-mediated VCP phosphorylation in the pathogenesis of IBM is suggested by several observations. First, our study shows that disease-causing VCP mutants have an impaired ability to interact with ASPL and an associated decrease in phosphorylation by ULK. As mentioned previously, ULK-mediated VCP phosphorylation is required for efficient SG disassembly (*3*). Second, mouse strains expressing disease-causing VCP mutants and those lacking ULK1/2 expression in muscle both develop a vacuolar myopathy with ubiquitin+/SQSTM1+/TDP43+ inclusions, similar to that observed in patients with IBM (*33*, *35*–*37*). The similar phenotypes caused by the expression of VCP mutants and ULK1/2 deficiency can be explained by the functional overlap between ULK and VCP in SG disassembly. The expression of VCP mutants or ULK1/2 deficiency that results in IBM-like pathology in mice impairs SG disassembly in cultured cells, resulting in the accumulation of poorly dynamic TDP43+ SGs (*4*, *27*). The functional importance of the ASPL-VCP interaction in mediating VCP phosphorylation by ULK is further supported by our observation that the SG disassembly defects in cells expressing disease-causing VCP mutants or VCP binding–defective ASPL mutants, both of which disrupt the ASPL-VCP interaction, were rescued by introducing phosphomimetic residues to bypass ULK-mediated phosphorylation. In light of this, the pathophysiological relevance of the ASPL-VCP interaction warrants further investigation in more physiologically relevant systems, such as patient-derived neurons, animal models, or chronic stress paradigms, which may better recapitulate the characteristic pathological accumulations of ubiquitin and SQSTM1 observed in MSP and related disorders.

One of the most intriguing results from our study was that despite the role of ASPL in SG disassembly, defects associated with the expression of pathogenic VCP variants, which failed to interact stably with ASPL, were negated by reducing endogenous levels of ASPL. Although the impaired SG assembly may have contributed to the neutralizing effect of *ASPL* knockdown, the SGs that did form failed to show a delay in resolution. This suggests that ASPL's role in promoting SG assembly is proportionally counterbalanced by its recruitment of ULK-activated VCP for SG disassembly, again highlighting the role of ASPL in coupling the assembly and disassembly of SGs. Further, our findings suggest that the uncoupling of these processes may reflect the mechanism by which a subset of pathogenic VCP mutations leads to the accumulation of poorly dynamic RNP granules and IBM-like disease. These observations lay the groundwork for exploring the therapeutic potential of manipulating ASPL levels and/or ULK activity in the treatment of MSP and related disorders.

Limitations of the study

While our study provides notable insights into ASPL's role in SG dynamics and regulation of VCP function, we acknowledge several limitations. First, although we validated certain findings using skeletal muscle from mice, most of our conclusions are based on in vitro and cell culture models. Future studies using additional cell types (e.g., primary cells and differentiated induced pluripotent stem cells), other stress conditions, and in vivo models should provide a more comprehensive understanding of ASPL's role in the dynamic regulation of SGs and other RNP granules.

Second, although our findings demonstrate that ASPL acts as a VCP cofactor for the disassembly of SGs, additional mechanisms likely contribute to this process, as SG disassembly is delayed but not completely abolished in cells with a disrupted ASPL-VCP interaction. ZFAND1 and FAF2 have been shown to regulate VCP-mediated SG disassembly under different stress conditions (*4*, *5*). Additional studies are required to determine the relative contributions of other VCP cofactors in the regulation of SG disassembly (in response to various stressors and in different cell types) and to what extent their functions are spatiotemporally related.

Last, this manuscript is focused on ASPL's role in SG disassembly and does not address its role(s) in other pathways involved in the resolution of SGs. Whereas disassembly is the primary mechanism responsible for the resolution of SGs formed in response to relatively short periods of exposure to stressors (e.g., 30- to 60-min HS or SA treatment) as were used in this study, autophagy has been implicated in the clearance of persistent SGs formed in response to more prolonged stresses (e.g., 90- to 120-min HS treatment) (*3*, *4*, *27*). ULK and VCP are required for the disassembly of SGs, a process that does not rely on other autophagy-related proteins. Nevertheless, as ULK and VCP are both involved in autophagy-related processes and autophagy has been implicated in the clearance of persistent SGs, our finding that ASPL is required for ULK-dependent activation of VCP warrants future studies examining the role of ASPL in autophagy-related processes.

MATERIALS AND METHODS

Experimental model and subject details

Animals

The *Aspl*$^{-/-}$ (also known as *Aspscr1*$^{-/-}$) mouse model was created using CRISPR-Cas9 technology and direct zygote microinjection in the Center for Advanced Genome Engineering (CAGE) at St. Jude Children's Research Hospital (St. Jude). Before embryo injection, chemically modified single guide RNAs (sgRNAs) were tested for editing efficiency in mouse Neuro-2A cells [American Type Culture Collection (ATCC)] stably expressing *Streptococcus pyogenes* (*Sp*Cas9) and assayed by targeted next-generation sequencing as previously described (*90*, *91*). For animal model generation, C57BL/6N female mice (the Jackson Laboratory), aged 3 to 4 weeks, were superovulated via gonadotrophin injections 1 and 2 days before the experiment: First, 5 U of gonadotrophin isolated from pregnant horses' serum was injected; then, 48 hours later, 5 U of human chorionic gonadotrophin was injected. Females were then mated to C57BL/6J males (the Jackson Laboratories). Fertilized zygotes were collected the following morning in M2 medium, and cumulus cells were stripped from the zygotes with hyaluronidase. Each zygote's pronucleus was microinjected with a mixture of *Sp*Cas9 mRNA (Trilink) at 10 ng/μl, sgRNA at 5 ng/μl (Synthego), and ssODN (single-stranded oligodeoxynucleotides) donors at 5 ng/μl (Integrated DNA Technologies) diluted in IDTE (a tris-EDTA buffer at pH 7.5). After maintenance in culture for 1 to 4 hours in M16 medium, the injected zygotes were transferred into the oviducts of day 0.5 pseudopregnant fosters (7- to 10-week-old CD-1 females from Charles River Laboratories mated to vasectomized CD-1 males). At 7 to 10 days of age, pups were sampled for genotyping, which was performed at the St. Jude CAGE. Positive animals were weaned at 21 days of age and bred to homozygosity. *Aspl*$^{-/-}$mice were backcrossed to C57BL/6 mice at least six generations before the experiments. Genome-editing reagents and primers used to create the *Asp1*$^{-/-}$ model are listed in table S2. All animal experiments were approved by the Institutional Animal Care and Use Committee (IACUC# 601-100574) at St. Jude Children's Research Hospital.

Cell culture

All cell lines used in this study are reported in table S2. U2OS (HTB-96) and HeLa (CCL-2) cells were purchased from ATCC. Genetically modified cells were generated using CRISPR-Cas9 technology in the St. Jude CAGE. Briefly, 300,000 to 400,000 HeLa or U2OS cells were transiently cotransfected with precomplexed RNPs consisting of 100 to 150 pmol of chemically modified sgRNA (Synthego), 33 to 50 pmol of 3× NLS *Sp*Cas9 protein (St. Jude Protein Production Core), 300 ng of pMaxGFP (Lonza), and, if required, 3 μg of ssODN donor or 1 μg of plasmid donor. The transfections were performed via nucleofection (4D-Nucleofector X Unit, Lonza) using the SE solution with the CN-114 (HeLa) program or the P3 solution with the CM-104 (U2OS) program in a 20-μl cuvette, according to the manufacturer's recommended protocol. Cells were sorted 5 days postnucleofection for GFP+ (transfected) or mRuby+ (tagged) single cells into 96-well plates containing prewarmed medium at the Flow Cytometry and Cell Sorting Shared Resource (St. Jude) and were clonally expanded. Clones were screened and verified for the desired modification with polymerase chain reaction–based assays and/or targeted deep sequencing. Resulting sequences were analyzed with CRIS.py as previously described (*90*, *91*). Selected clones were tested negative for mycoplasma by the MycoAlert Plus Mycoplasma Detection Kit (Lonza) and authenticated using the PowerPlex Fusion System (Promega), performed at the Hartwell Center (St. Jude). Editing construct sequences and screening primers are listed in table S2. The G3BP-tdTomato knock-in, enhanced GFP (EGFP)–TIA1 knock-in, G3BP1-mRuby3/TDP43 EGFP dual knock-in U2OS cells, and U2OS cells stably expressing GFP-G3BP and G3BP-GFP have been described previously (*3*, *14*, *59*, *90*, *91*).

To generate G3BP-tdTomato knock-in U2OS cells that stably express WT or mutant forms of ASPL, HEK293T (CRL-3216) cells were first transfected with the N174 lentiviral vector (Addgene, #31822) containing different ASPL cDNAs along with packaging vectors PSPAX2 and PMD2.g using Lipofectamine 2000 (Thermo Fisher Scientific). Supernatants were collected from the HEK293T cultures 48 hours after transfection. U2OS cells were then incubated with cell-free lentiviral supernatants containing polybrene (8 μg/ml; Santa Cruz Biotechnology); positively transduced cells were sorted on the basis of GFP expression. A similar protocol was used to generate GFP-G3BP U2OS cells stably expressing WT or mutant forms of VCP (cloned in SJL12 MND-mTagBFP vector). Positively transduced cells were sorted by blue fluorescent protein (BFP) fluorescence and expanded further for subsequent experiments. All cells were cultured in Dulbecco's modified Eagle's medium (DMEM) (Thermo Fisher Scientific) supplemented with 10% fetal bovine serum (FBS; HyClone Laboratories Inc.), penicillin/streptomycin (Thermo Fisher Scientific), and GlutaMAX (Thermo Fisher Scientific) at 37°C (5% CO_2), unless otherwise stated.

Plasmid, siRNA, and transfection

All plasmids used in this study are reported in the table S2. Plasmids expressing ULK1-DDK (FLAG) and VCP were described previously (*3*). pCMV-DDK-mouse Aspscr1 was purchased from Origene. EGFP-ASPSCR1 was a gift from R. Hartmann-Petersen, Department of Biology, University of Copenhagen, Copenhagen, Denmark (*92*). Constructs carrying point mutations were generated using the New England Biolabs Q5 Site-Directed Mutagenesis Kit or Agilent Technologies QuikChange II site-directed mutagenesis kit per the manufacturers' instructions. To generate lentiviral constructs, the cDNA of WT or mutant ASPL was amplified using Phusion high-fidelity DNA polymerase and cloned into an N174 vector (Addgene, #31822) using the standard restriction digestion/ligation procedure. The cDNA of *VCP* was amplified using Phusion high-fidelity DNA polymerase (New England Biolabs) with T2A sites in the reverse primer and cloned into an SJL12 MND-mTagBFP vector (St. Jude Vector Laboratory) by restriction digestion/ligation.

For transient overexpression of plasmids carrying cDNA, cells were transfected with Lipofectamine 2000 (Thermo Fisher Scientific) according to the manufacturer's instructions, and experiments were performed at 48 hours posttransfection. Knockdown experiments were performed using Lipofectamine RNAiMax (Thermo Fisher Scientific) via standard reverse transfection procedures with the nontargeting pool, ASPL, VCP, ULK1, and ULK2 siRNA constructs (Horizon Discovery).

The plasmid for expressing recombinant G3BP protein in bacteria was described previously (*14*). The plasmids for expressing recombinant WT or truncated ASPL were cloned into a pGEX-2T-TEV (tobacco etch virus) vector using standard cloning procedures.

Live-cell imaging and FRAP assays

Live-cell imaging and FRAP assays were performed as described previously (*4*). Cells were cultured in glass bottom dishes (ibidi, Gräfelfing), and multipoint images over 10 XY fields were acquired every 1 min using a 60× Plan Apo 1.4 numerical aperture (NA) Nikon oil objective (Nikon) and Perfect Focus 2.0 engaged on the CSU W1 Confocal Scanner Unit (Yokogawa) attached to a Nikon ECLIPSE Ti2 microscope with a Photometrics Prime 95B camera (Teledyne Photometrics). Nikon NIS-Elements 5.21 was used to acquire time-lapse live-cell imaging and FRAP. The cells were maintained at 37°C and 5% CO_2 using a Bold Line Cage Incubator (Okolab) and an objective heater (Bioptechs). The cells were heat shocked at 43°C for 30 min (G3BP-tdTomato knock-in cell line) or 1 hour (G3BP-GFP overexpression cell line) by raising the temperature of the objective heater and were then allowed to recover at 37°C for 1 hour. The images were acquired every 1 min for 1.5 to 2 hours. The experiment was performed in two biological replicates. After thresholding the images using the Fiji software (*93*), SG area was normalized to cytoplasmic area and plotted using GraphPad Prism 9.

To perform FRAP assays, time-lapse images were acquired every 100 ms, over the course of 35 s, using a 488-nm FRAP laser for 2 s to photobleach the SGs. Measurements were taken from at least 15 SGs from 15 different cells for each condition. The mean fluorescence intensity in the regions of interest (ROIs) of the photobleached region, a nonphotobleached region, and the background for each time-lapse were extracted using NIS-Elements 5.21. Single SGs were bleached and analyzed. The experiment was performed in two biological replicates. The values retrieved from the ROIs were exported into Igor Pro 7.0 (WaveMetrics), and individual fit curves were generated, with means ± SEM displayed.

Immunofluorescence microscopy

Cells (HEK293T, U2OS, or HeLa) grown in glass-bottom dishes (ibidi) were fixed using 4% formaldehyde (Polysciences) and permeabilized using 0.5% Triton X-100 (Sigma-Aldrich). After blocking in 2% goat serum (Thermo Fisher Scientific), the cells were incubated with primary antibodies overnight. The next day, cells were washed three times with phosphate-buffered saline with Tween (PBS-T) and then incubated with secondary antibodies conjugated to AF488, AF555, or AF647 (Invitrogen) before being mounted with ProLong Gold

Antifade Mountant with 4′,6-diamidino-2-phenylindole (DAPI; Thermo Fisher Scientific). The images were then captured using a 60× Plan Apo 1.4 NA Nikon oil objective (Nikon) on a Nikon A1R point scanning confocal attached to a Nikon ECLIPSE Ti2 stand.

Immunoblot assay

HEK293T/U2OS/mouse embryonic fibroblast (MEF) cells were washed in 1× PBS buffer, followed by lysis in radioimmunoprecipitation assay buffer (Thermo Fisher Scientific) supplemented with protease inhibitor cocktail (Roche Diagnostics) and phosphatase inhibitor cocktail (Roche Diagnostics). After incubation for 20 min on ice, lysates were centrifuged at 20,000*g* for 20 min at 4°C. Then, 4× Laemmli SDS buffer (Thermo Fisher Scientific) was added to the supernatant, and samples were boiled at 95°C for 10 min. The samples were then loaded onto SDS–polyacrylamide gel electrophoresis (PAGE) (NuPAGE 4 to 12%, bis-tris, Thermo Fisher Scientific) and then, after transfer to polyvinylidene difluoride (PVDF) membranes (Thermo Fisher Scientific), incubated overnight at 4°C with primary antibodies. The next day, membranes were washed three times with PBS-T (0.05% Tween) and further incubated with anti-rabbit or anti-mouse secondary antibodies at a dilution of 1:10,000 for 1 hour at room temperature (20° to 25°C). The blots were developed using a chemiluminescence reagent (Cytiva) and quantified using Fiji software (*93*) .

Coimmunoprecipitation assay

HEK293T/U2OS/MEF cells were lysed in an immunoprecipitation buffer (Thermo Fisher Scientific) supplemented with a protease inhibitor cocktail (Roche Diagnostics) and a phosphatase inhibitor cocktail (Roche Diagnostics). After incubation for 30 min on ice, the lysates were centrifuged at 20,000*g* for 20 min at 4°C, and the supernatants were incubated with the indicated rabbit or mouse immunoglobulin G (IgG) antibodies, along with protein G beads (Cytiva). The next day, after three washes with the same immunoprecipitation buffer, the beads were boiled at 95°C for 20 min in a 2× Laemmli SDS buffer. The samples were then loaded onto SDS-PAGE gel, followed by immunoblot analysis.

Blue native PAGE assay

The blue native PAGE assay was performed according to a previously published protocol (*94*). HEK293T cells overexpressing GFP, GFP-ASPL, GFP-D351A ASPL, or GFP-PPAA ASPL were washed in PBS and solubilized in an 8:1 ratio of protein/digitonin (Thermo Fisher Scientific). After centrifugation, the supernatants were mixed with Coomassie G-250 (SERVA) and loaded onto a native PAGE gel (Thermo Fisher Scientific). After transferring the native PAGE gel to a PVDF membrane (Thermo Fisher Scientific), the PVDF membrane was immunoblotted with VCP antibodies. HeLa cells expressing the C-terminal Flag knock-in of ASPL, along with the siRNA targeting VCP or nontargeting control siRNAs, were washed and solubilized according to the procedure described above and subjected to immunoprecipitation using anti-Flag M2 beads (MilliporeSigma). The immunoprecipitants were eluted using the 3×-Flag peptide (MilliporeSigma), mixed with Coomassie G-250, and loaded on to the native PAGE gel. After transfer, the PVDF membrane was probed with Flag and VCP antibodies. The experiment was repeated twice.

NanoBiT assay

The NanoBiT assay (Promega) was performed according to the manufacturer's instructions. HEK293T cells were transfected with siRNA against ASPL and with plasmids expressing ULK1-LgBiT, VCP-SmBiT, GFP, WT GFP-ASPL, or mutant GFP-ASPL using Lipofectamine 2000. After treatment with SA (Sigma-Aldrich) for 1 hour, the luminescence reagent (25 μl) was added to the wells, and readings were recorded using an EnSpire multimode plate reader with a 2-s integration time.

Protein purification

Full-length and mutant G3BP were expressed in *Escherichia coli* Rosetta 2(DE3) cells (Millipore) and purified under native conditions, as described previously (*14*). Full-length human ASPL and its deletions were expressed and purified from recombinant bacterial BL21 gold (DE3) cells. *E. coli* cells were then grown to an optical density at 600 nm of 0.8 and induced with 0.6 mM IPTG (isopropyl-β-D-thiogalactopyranoside) at 16°C overnight. The bacterial pellets were resuspended in buffer [50 mM tris (pH 7.5), 500 mM NaCl, 2 mM 2-mercaptoethanol, and 30 mM imidazole]. After sonication, the supernatant was centrifuged at 17,000*g* for 30 min at 4°C. Supernatants were applied to packed Ni–nitrilotriacetic acid resin equilibrated with resuspension buffer. Proteins were eluted by adding an elution buffer [50 mM tris (pH 7.5), 500 mM NaCl, 2 mM 2-mercaptoethanol, and 500 mM imidazole]. The eluted proteins were incubated with TEV protease with a cleavage buffer [50 mM tris (pH 7.5) and 5 mM 2-mercaptoethanol] at 4°C overnight. Proteins were treated with ribonuclease A (RNase A) (0.1 mg/ml; Thermo Fisher Scientific) to remove RNA. The proteins were then purified using a Superdex 200 16/200 column (GE Healthcare) equilibrated in size exclusion chromatography buffer [25 mM sodium phosphate (pH 7.5), 50 mM NaCl, 1 mM EDTA, and 2 mM TCEP]. Last, the fractions were analyzed via SDS-PAGE, pooled, concentrated, filtered, flash frozen in liquid nitrogen, and stored at −80°C.

Liquid-liquid phase separation

In vitro LLPS experiments were conducted according to previously published procedures (*14*). The assays were carried out at room temperature (20° to 25°C), unless specified otherwise. To induce LLPS of G3BP, indicated concentrations of either Ficoll 400 or RNA were added. The samples were combined in low-binding tubes (COSTAR 3206) and transferred to a sandwiched chamber formed by a coverslip and a glass slide with a double-sided spacer (Sigma-Aldrich, GBL654002). We observed the samples using differential interference contrast (DIC) settings on a Leica widefield microscope equipped with a 20× objective. All images were captured within 5 min after LLPS induction. When RNA was included in the trial, we isolated total RNA from U2OS cells using TRIzol and determined the RNA concentration using a NanoDrop spectrophotometer (Thermo Fisher Scientific). Proteins were labeled using the Invitrogen Alexa Fluor protein labeling kits as per the manufacturer's instructions.

Cell lysis and induction of LLPS from lysates

The reconstitution of SGs in mammalian cell line lysates was performed as described previously (*59*). U2OS cells stably expressing G3BP1-GFP or U2OS cells in which TIA1, caprin 1, TDP43, or G3BP1 had either GFP or mRuby3 stably encoded into their endogenous C-terminal loci using CRISPR-Cas9 were cultured in DMEM (Invitrogen, 11995-065) supplemented with 10% FBS, penicillin/streptomycin (Invitrogen), and GlutaMAX (Invitrogen) at 37°C (5% CO_2). Cells were treated with either siCtrl or si*ASPL*. After 48 hours of transfection, cell pellets were lysed gently in 250 μl of lysis buffer [50 mM tris-HCl (pH 7.0), 0.5% NP-40, protease inhibitor cocktail

(Roche Diagnostics), and 2.5% murine RNase inhibitor]. The lysates were centrifuged at room temperature (20° to 25°C) for 5 min at 21,000*g*. The supernatants from the lysates were transferred to a new tube and combined with various concentrations of purified proteins [G3BP/ASPL/bovine serum albumin (BSA)] to induce LLPS. Immediately after mixing, samples were placed into imaging vessels, and LLPS was observed using a 60× Plan Apo 1.4 NA Nikon oil objective (Nikon) on a CSU W1 Confocal Scanner Unit (Yokogawa) attached to a Nikon ECLIPSE Ti2 microscope with a Photometrics Prime 95B camera (Teledyne Photometrics).

Determination of protein concentrations in cell lysates

The HeLa and U2OS cells were grown on a 60-mm dish and were lysed using 200 μl of lysis buffer (Thermo Fisher Scientific). Increasing amounts of purified ASPL, G3BP, and VCP were loaded onto SDS-PAGE gels alongside lysates prepared from HeLa and U2OS cells. After electrophoresis, proteins were transferred to PVDF membranes, which were then probed with antibodies specific to ASPL, G3BP, and VCP. To determine protein concentrations, a standard curve was generated by quantifying the band intensities of the recombinant proteins using Fiji software (*93*). The intensity values were fitted to a linear equation to calculate the concentrations of the target proteins in the cell lysates. The experiment was performed in triplicate, and the average protein concentrations from the three replicates were reported in figs. S5F and S6I.

GST pull-down

GST control and GST-G3BP proteins were mixed with full-length ASPL, ASPLΔUBL, or ASPLΔUBX+ in a 500-μl final reaction volume at a final concentration of 100 nM. This mixture was then incubated for 1 hour at room temperature (20° to 25°C) in a pull-down buffer [50 mM Hepes (pH 7.5), 150 mM NaCl, 0.1% Triton X-100, and 1 mM dithiothreitol (DTT)]. Complexes were pulled down using Glutathione Sepharose 4B resin (Cytiva) for 2 hours at 4°C. They were then washed three times with a wash buffer [50 mM Hepes (pH 7.5), 150 mM NaCl, 0.1% Triton X-100, and 1 mM DTT] and analyzed via immunoblot using anti-GST and anti-ASPL antibodies.

ThT staining

Purified recombinant proteins (G3BP, BSA, WT ASPL, and ASPL truncations) were incubated with a final concentration of 5 μM ThT at room temperature (20° to 25°C). All images were captured within 5 min using the 488-nm channel on a Leica widefield microscope.

Modeling the probability of SG formation as a function of G3BP-GFP levels

U2OS *G3BP1/2* DKO cells were transfected with WT GFP-G3BP1. Cells were exposed to 300 μM SA for 30 min, fixed with 4% paraformaldehyde, and imaged using the BioTek Cytation C10 Confocal Imaging Reader (Agilent). SG formation and GFP intensities were assessed in individual cells. Ordinary logistic regression was used to model the probability of SG formation in each cell as a function of GFP intensity and estimate the GFP intensity at which the probability of SG formation was 50%. Confidence intervals and *P* values were computed by repeating these calculations for each 1000 bootstrap datasets obtained by randomly resampling cells with replacement (*95*).

Proteomics and analysis

Sample preparation and MS

Proteins in gel bands were reduced with DTT (Sigma-Aldrich) and alkylated using iodoacetamide (Sigma-Aldrich). The gel bands were then excised, washed, dried, and rehydrated with a buffer containing trypsin (Promega). Samples were digested overnight and acidified, and then the peptides were extracted. The extracts were dried and reconstituted in 5% formic acid. The peptide samples were loaded on a nanoscale capillary reverse-phase C18 column using a high-performance LC (HPLC) system (Thermo Fisher Scientific UltiMate3000) and eluted by a gradient. The eluted peptides were ionized and detected by an inline mass spectrometer (Thermo Fisher Scientific Orbitrap Exploris 480). The MS and MS/MS spectra were collected over a 75-min LC gradient.

For analyses of protein compositions in lysate granules, lysate granules were induced as previously described (*59*) by increasing the concentration of indicated lysate by either 20 μM purified G3BP or 20 μM purified ASPL. Mock purifications without the addition of purified protein were used as controls. SGs were allowed to form for 40 min, and granules were isolated from the lysate by centrifugation at 2000*g* for 5 min. The resulting granules were collected in 2× LDS sample buffer and separated by SDS-PAGE. Proteins were isolated from the gel and digested with trypsin overnight. Samples were loaded on a nanoscale capillary reverse-phase C18 column by an HPLC system (Thermo Fisher Scientific Ultimate 3000) and eluted by a gradient (~90 min). Eluted peptides were ionized by electrospray ionization and detected by an inline mass spectrometer (Thermo Fisher Scientific Orbitrap Fusion). Database searches were performed using SEQUEST search engine using an in-house SPIDERS software package. MS/MS spectra were filtered by mass accuracy and matching scores to reduce protein FDR to ~1%. The total number of spectral counts for each protein identified was reported by sample. Proteins were determined to be present in lysate granules if they were found to be enriched at greater than threefold in the granule versus mock samples and had at least two separate peptides identified by LC-MS/MS.

Database searches and analyses

Database searches were performed using the JUMP (*96*) search engine against a composite target/decoy UniProt human protein database (*97*). All matched MS/MS spectra were filtered by mass accuracy and matching scores to reduce the protein FDR to <1%. Spectral counts matched to individual proteins reflect their relative abundance in one sample after the protein size was normalized. The spectral counts between samples for a given protein were used to calculate the *P* value, which was derived using a *G* test (*98*). GO analyses were conducted using the DAVID (Database for Annotation, Visualization, and Integrated Discovery) Bioinformatics Resource. Table S1C presents the FDRs for selected GO terms within each Venn diagram subset. Table S1E summarizes the GO biological process, cellular component, and molecular function terms with the lowest FDR for each Venn diagram subset.

FRAP of G3BP condensates and ASPL variants in vitro

All in vitro FRAP measurements were carried out on the FRAP module installed on LAS X software, using a STELLARIS 5 confocal microscope platform configured on a DMi8 inverted microscope (Leica). All samples were prepared in 50 mM Hepes (pH 7.5), 150 mM NaCl, and 10% Ficoll 70 at the indicated protein concentrations with the addition of 100 nM G3BP labeled with AF488 or 100 nM of the

indicated ASPL variant labeled with AF555. Bleaching was performed on a circular ROI ~1 μm in diameter with 100% laser power at peak excitation wavelength for the given fluorophore to result in bleaching to ~10% of prebleached fluorescence intensity. Recovery of the bleached region was monitored every 0.745 s for a total of 90 s. Intensity values were normalized by dividing by values of an unbleached condensate in the same field of view to account for general photobleaching and then dividing by the resulting maximum value to set the highest intensity to 1. Plots were generated in GraphPad Prism 10 and represent means and SDs from three technical replicates.

Partition coefficients of G3BP and ASPL variants within G3BP condensates

All images used to calculate partitioning were captured on a STELLARIS 5 confocal microscope platform configured on a DMi8 inverted microscope, controlled through LAS X software (Leica). All samples were prepared in 50 mM Hepes (pH 7.5), 150 mM NaCl, and 10% Ficoll 70 at the indicated protein concentrations with the addition of 100 nM G3BP labeled with AF488 and 100 nM of the indicated ASPL variant labeled with AF555. Partitioning of AF488-labeled G3BP and AF555-labeled ASPL variants was calculated as the ratio of intensity values within condensates divided by the average background intensity determined from five randomly chosen background regions. Plots were generated in GraphPad Prism 10 and represent means and SDs of partitioning within 10 condensates from each of three technical replicates.

Viscosity estimation from video particle tracking–based nanorheology of ASPL-treated G3BP condensates

Video particle tracking–based nanorheology was performed to estimate the viscosity of the G3BP condensates treated with WT ASPL, ΔUBX+ ASPL, and UBX+ alone variants of ASPL. Ten percent of Ficoll 70 was used to induce the phase separation of G3BP condensates under 50 mM Hepes (pH 7.5) and 150 mM NaCl buffer conditions. To understand the dose-dependent changes in the material properties of G3BP condensates upon the addition of ASPL variants, heterotypic condensates of G3BP-ASPL variants were formed by adding 5 and 25 μM of the ASPL variants during the sample preparation. Yellow-green fluorescent carboxylate-modified 200-nm beads, mixed during the sample preparation, were used as probe particles for nanorheology. For measurements, the samples were drop casted on Tween 20–coated coverslips and were subsequently sandwiched with a glass slide chamber using double-sided tape.

The motion of the beads diffusing inside the condensates was acquired in the form of videos using epifluorescence microscopy performed with a Zeiss primovert inverted microscope with a 100× oil-immersion objective lens. Teledyne FLIR blackfly S USB3 complementary metal-oxide semiconductor camera was used to capture videos having 1000 frames with 100-ms exposure time resulting in an acquisition rate of 10 frames/s. The details of the analysis performed to obtain the MSD of the beads are described elsewhere (*64*). Briefly, these videos were used to get the trajectories in two dimensions of each bead inside the condensate using the TrackMate plugin of Fiji software (*93*, *99*). The intensity filters in TrackMate were used to ensure that only single beads were tracked, and aggregates were avoided during tracking.

These trajectories were used to estimate the center of mass (COM) vector **R** at each time point using

$$\mathbf{R}_{\mathrm{COM}}(k) = \mathbf{R}_0 + \sum_{k=0}^{k}\left(\frac{1}{N_k}\sum_{i=1}^{N}\mathbf{v}_{i,k}\right)\Delta k \quad (1)$$

Here, $\mathbf{R}_0$ is the initial COM vector, $\mathbf{v}_{i,k}$ is the velocity of the particle i in frame k, and N_k is the number of particles in the frame k. This COM vector **R** is then subtracted from the individual bead trajectories to correct any possible sample drift during data acquisition. The COM vectors at each time point were then used to compute the ensemble-averaged MSDs of the beads inside the condensates using

$$\mathrm{MSD}(\tau) = \langle \mathbf{R}(t+\tau) - \mathbf{R}(t)\rangle_{t,N} \quad (2)$$

where τ is the lag time between the frames. The representative ensemble-averaged MSDs for G3BP1 condensates and the condensates formed from G3BP1 and ASPL variants mixtures are shown in Fig. 3 (J and K). Fitting the time-averaged MSDs to a power law

$$\mathrm{MSD}(\tau) = 4D\tau^{\alpha} + N \quad (3)$$

we estimated the diffusion coefficients of the beads inside the condensates. In Eq. 3, D is the diffusion coefficient, α is the diffusivity parameter characteristic of the diffusion type of the beads, and N is a correction factor accounting for the noise during tracking. The case $\alpha \rightarrow 1$ at long lag times signifies that the fluid is terminally viscous. After assuring this characteristic for the extracted MSDs for the beads, the Stokes-Einstein equation (*64*)

$$\eta = \frac{k_{\mathrm{B}}T}{6\pi DR} \quad (4)$$

was used to estimate the terminal viscosity of the beads diffusing inside the condensates, where r is the radius of the particle, k_{B} is the Boltzmann constant, and T is the temperature in kelvin. We reported the average of the terminal viscosities determined over six different condensates from two independent sample preparations in Fig. 3J.

Fluorescence-detected sedimentation velocity analytical ultracentrifugation

Purified ASPL protein was buffer exchanged in 50 mM Hepes and 200 mM NaCl and concentrated to 2.5 mg/ml. Dimethyl sulfoxide (50 μl) was added to 1 mg of AF488 (AF488 carboxylic acid, succinimidyl ester from Invitrogen). The AF488 solution was then added to the protein, and the mixture was incubated at room temperature (20° to 25°C) for 1 hour. After incubation, the mixture was passed over a PD MiniTrap G-25 column (Cytiva) to separate the labeled protein from the excess dye. Labeling efficiency was determined by measuring the ratio of protein concentration to fluorescein concentration measured at 495 nm. The labeling efficiency of AF488-ASPL was measured at ≥80%.

FDS-SV experiments were conducted in a ProteomeLab XL-I analytical ultracentrifuge (Beckman Coulter, Indianapolis, IN) with an An-50 Ti eight-hole rotor with the fluorescence detective system (AVIV Biomedical), following standard protocols unless mentioned otherwise (*100*–*102*). Two samples, AF488-ASPL alone (final concentration of 0.2 μM) and AF488-ASPL (final concentration of 0.2 μM) in a mixture with VCP (final concentration of 16.8 μM), in 50 mM Hepes, 200 mM NaCl, 2 mM adenosine 5′-triphosphate (ATP), 2 mM $MgCl_2$, and 0.5 mM sodium vanadate buffer were loaded into cell assemblies with double-sector 12-mm charcoal-filled centerpieces and quartz windows. The cell assemblies, containing sample volumes of ~320 μl, were placed in the rotor. For the FDS-SV experiments, radial calibration and the setup of focusing depth and photomultiplier tube (PMT) voltage were performed at 3000 rpm. The focal depth was set

at 4.696 mm. Sufficient fluorescent signal for the samples with similar concentration of the fluorescent-labeled protein was obtained with a PMT setting of 40 to 65% and gain at 1. The concentration of fluorescent-labeled protein, AF488-ASPL, at 0.2 μM, did not require BSA as carrier protein as is customary for concentration in the nanomolar range. The temperature equilibrium was carried out at 20°C for 2 hours at rest, followed by acceleration from 0 to 45,000 rpm. Fluorescence scans were collected continuously for 10 to 12 hours.

The fluorescence-detected velocity data were analyzed with the diffusion-deconvoluted sedimentation coefficient distribution model $c(s)$ in SEDFIT (http://sedfitsedphat.nibib.nih.gov/software) using algebraic noise decomposition (*100*–*102*). The signal-average frictional ratio and meniscus position were refined with nonlinear regression, and maximum entropy regularization was applied at a confidence level of $P = 0.68$.

Buffer density and viscosity at 20°C were calculated using the software SEDNTERP (www.jphilo.mailway.com/download.htm) (*103*). The density and viscosity of the buffer at 20°C were also measured using a densitometer model DMA 5000 M and a microviscometer model AMVn, respectively (both from Anton Paar Inc., Ashland, VA). The partial specific volumes and molecular masses of the proteins were calculated on the basis of their amino acid compositions in SEDFIT (http://sedfitsedphat.nibib.nih.gov/software).

The same sedimentation velocity (sv) profiles (fluorescence intensity) of AF488-ASPL (final concentration of 0.2 μM) in a mixture with VCP (final concentration of 16.8 μM) in 50 mM Hepes, 200 mM NaCl, 2 mM ATP, 2 mM $MgCl_2$, and 0.5 mM sodium vanadate buffer were also fitted to a two-dimensional size-and-shape distribution, $c(s,f/f_0)$ (with one dimension representing the s distribution and the other the f/f_0 distribution) model. The linear s grid from 1 to 20 S with 100 s values and an equidistant f/f_0 grid of 0.25 steps from 0.5 to 3.0 were calculated. Tikhonov-Phillips regularization at 1 SD. The velocity data were also transformed to $c(s,f/f_0)$, $c(M,f/f_0)$, and $c(s,R)$ distributions with M as the molar mass (in daltons), R as the Stokes radius (in nanometers), f/f_0 as the frictional ratio, and s as the sedimentation coefficient (in siemens) and plotted as contour plots. The color temperature of the contour lines indicates the population of species. These distributions were not normalized (*100*, *104*). All plots were created in GUSSI (www.utsouthwestern.edu/labs/mbr/software/) (*105*).

Statistical methods and analysis

All quantitative data are shown as means ± SEM, unless otherwise specified. Statistical significance was determined by a two-tailed Student's t tests for two-component comparisons and by an analysis of variance (ANOVA) with post hoc Tukey's, Sidak's, or Dunnett's test, as appropriate for multicomponent comparisons using GraphPad Prism 9. The significance of the curves showing the area occupied by SGs normalized to the total cytoplasmic area was determined by comparing the area under the curves using an unpaired t test in GraphPad Prism 9. The exact value of n is indicated in each figure legend. Differences were considered statistically significant if $^*P \leq 0.05$, $^{**}P \leq 0.01$, $^{***}P \leq 0.001$, and $^{****}P \leq 0.0001$. All statistical parameters are also reported in each figure and figure legend.

Supplementary Materials

The PDF file includes:
Figs. S1 to S7
Legends for tables S1 and S2
Legends for movies S1 to S7

Other Supplementary Material for this manuscript includes the following:
Tables S1 and S2
Movies S1 to S7

REFERENCES AND NOTES

1. D. S. W. Protter, R. Parker, Principles and properties of stress granules. *Trends Cell Biol.* **26**, 668–679 (2016).
2. S. Hofmann, N. Kedersha, P. Anderson, P. Ivanov, Molecular mechanisms of stress granule assembly and disassembly. *Biochim. Biophys. Acta Mol. Cell Res.* **1868**, 118876 (2021).
3. B. Wang, B. A. Maxwell, J. H. Joo, Y. Gwon, J. Messing, A. Mishra, T. I. Shaw, A. L. Ward, H. Quan, S. M. Sakurada, S. M. Pruett-Miller, T. Bertorini, P. Vogel, H. J. Kim, J. Peng, J. P. Taylor, M. Kundu, ULK1 and ULK2 regulate stress granule disassembly through phosphorylation and activation of VCP/p97. *Mol. Cell* **74**, 742–757.e8 (2019).
4. Y. Gwon, B. A. Maxwell, R. M. Kolaitis, P. Zhang, H. J. Kim, J. P. Taylor, Ubiquitination of G3BP1 mediates stress granule disassembly in a context-specific manner. *Science* **372**, eabf6548 (2021).
5. A. Turakhiya, S. R. Meyer, G. Marincola, S. Böhm, J. T. Vanselow, A. Schlosser, K. Hofmann, A. Buchberger, ZFAND1 recruits p97 and the 26S proteasome to promote the clearance of arsenite-induced stress granules. *Mol. Cell* **70**, 906–919.e7 (2018).
6. M. Ganassi, D. Mateju, I. Bigi, L. Mediani, I. Poser, H. O. Lee, S. J. Seguin, F. F. Morelli, J. Vinet, G. Leo, O. Pansarasa, C. Cereda, A. Poletti, S. Alberti, S. Carra, A surveillance function of the HSPB8-BAG3-HSP70 chaperone complex ensures stress granule integrity and dynamism. *Mol. Cell* **63**, 796–810 (2016).
7. S. F. Banani, H. O. Lee, A. A. Hyman, M. K. Rosen, Biomolecular condensates: Organizers of cellular biochemistry. *Nat. Rev. Mol. Cell Biol.* **18**, 285–298 (2017).
8. Y. Lin, D. S. Protter, M. K. Rosen, R. Parker, Formation and maturation of phase-separated liquid droplets by RNA-binding proteins. *Mol. Cell* **60**, 208–219 (2015).
9. B. Wang, G. Pareek, M. Kundu, ULK/Atg1: Phasing in and out of autophagy. *Trends Biochem. Sci.* **49**, 494–505 (2024).
10. S. Jain, J. R. Wheeler, R. W. Walters, A. Agrawal, A. Barsic, R. Parker, ATPase-modulated stress granules contain a diverse proteome and substructure. *Cell* **164**, 487–498 (2016).
11. S. Markmiller, S. Soltanieh, K. L. Server, R. Mak, W. Jin, M. Y. Fang, E. C. Luo, F. Krach, D. Yang, A. Sen, A. Fulzele, J. M. Wozniak, D. J. Gonzalez, M. W. Kankel, F. B. Gao, E. J. Bennett, E. Lécuyer, G. W. Yeo, Context-dependent and disease-specific diversity in protein interactions within stress granules. *Cell* **172**, 590–604.e13 (2018).
12. J. Y. Youn, W. H. Dunham, S. J. Hong, J. D. R. Knight, M. Bashkurov, G. I. Chen, H. Bagci, B. Rathod, G. MacLeod, S. W. M. Eng, S. Angers, Q. Morris, M. Fabian, J. F. Côté, A. C. Gingras, High-density proximity mapping reveals the subcellular organization of mRNA-associated granules and bodies. *Mol. Cell* **69**, 517–532.e11 (2018).
13. H. Marmor-Kollet, A. Siany, N. Kedersha, N. Knafo, N. Rivkin, Y. M. Danino, T. G. Moens, T. Olender, D. Sheban, N. Cohen, T. Dadosh, Y. Addadi, R. Ravid, C. Eitan, B. T. Cohen, S. Hofmann, C. L. Riggs, V. M. Advani, A. Higginbottom, J. Cooper-Knock, J. H. Hanna, Y. Merbl, L. Van Den Bosch, P. Anderson, P. Ivanov, T. Geiger, E. Hornstein, Spatiotemporal proteomic analysis of stress granule disassembly using APEX reveals regulation by SUMOylation and links to ALS pathogenesis. *Mol. Cell* **80**, 876–891.e6 (2020).
14. P. Yang, C. Mathieu, R. M. Kolaitis, P. Zhang, J. Messing, U. Yurtsever, Z. Yang, J. Wu, Y. Li, Q. Pan, J. Yu, E. W. Martin, T. Mittag, H. J. Kim, J. P. Taylor, G3BP1 is a tunable switch that triggers phase separation to assemble stress granules. *Cell* **181**, 325–345.e28 (2020).
15. D. W. Sanders, N. Kedersha, D. S. W. Lee, A. R. Strom, V. Drake, J. A. Riback, D. Bracha, J. M. Eeftens, A. Iwanicki, A. Wang, M. T. Wei, G. Whitney, S. M. Lyons, P. Anderson, W. M. Jacobs, P. Ivanov, C. P. Brangwynne, Competing protein-RNA interaction networks control multiphase intracellular organization. *Cell* **181**, 306–324.e28 (2020).
16. J. Guillén-Boixet, A. Kopach, A. S. Holehouse, S. Wittmann, M. Jahnel, R. Schlüßler, K. Kim, I. Trussina, J. Wang, D. Mateju, I. Poser, S. Maharana, M. Ruer-Gruß, D. Richter, X. Zhang, Y. T. Chang, J. Guck, A. Honigmann, J. Mahamid, A. A. Hyman, R. V. Pappu, S. Alberti, T. M. Franzmann, RNA-induced conformational switching and clustering of G3BP drive stress granule assembly by condensation. *Cell* **181**, 346–361.e17 (2020).
17. S. F. Banani, A. M. Rice, W. B. Peeples, Y. Lin, S. Jain, R. Parker, M. K. Rosen, Compositional control of phase-separated cellular bodies. *Cell* **166**, 651–663 (2016).
18. A. S. Lyon, W. B. Peeples, M. K. Rosen, A framework for understanding the functions of biomolecular condensates across scales. *Nat. Rev. Mol. Cell Biol.* **22**, 215–235 (2021).
19. P. K. Sahoo, S. J. Lee, P. B. Jaiswal, S. Alber, A. N. Kar, S. Miller-Randolph, E. E. Taylor, T. Smith, B. Singh, T. S. Ho, A. Urisman, S. Chand, E. A. Pena, A. L. Burlingame, C. J. Woolf, M. Fainzilber, A. W. English, J. L. Twiss, Axonal G3BP1 stress granule protein limits axonal mRNA translation and nerve regeneration. *Nat. Commun.* **9**, 3358 (2018).
20. C. Bussi, A. Mangiarotti, C. Vanhille-Campos, B. Aylan, E. Pellegrino, N. Athanasiadi, A. Fearns, A. Rodgers, T. M. Franzmann, A. Saric, R. Dimova, M. G. Gutierrez, Stress granules plug and stabilize damaged endolysosomal membranes. *Nature* **623**, 1062–1069 (2023).
21. F. Zappa, C. Wilson, G. Di Tullio, M. Santoro, P. Pucci, M. Monti, D. D'Amico, S. Pisonero-Vaquero, R. De Cegli, A. Romano, M. A. Saleem, E. Polishchuk, M. Failli,

L. Giaquinto, M. A. De Matteis, The TRAPP complex mediates secretion arrest induced by stress granule assembly. *EMBO J.* **38**, e101704 (2019).
22. K. Thedieck, B. Holzwarth, M. T. Prentzell, C. Boehlke, K. Klasener, S. Ruf, A. G. Sonntag, L. Maerz, S. N. Grellscheid, E. Kremmer, R. Nitschke, E. W. Kuehn, J. W. Jonker, A. K. Groen, M. Reth, M. N. Hall, R. Baumeister, Inhibition of mTORC1 by astrin and stress granules prevents apoptosis in cancer cells. *Cell* **154**, 859–874 (2013).
23. M. Paget, C. Cadena, S. Ahmad, H. T. Wang, T. X. Jordan, E. Kim, B. Koo, S. M. Lyons, P. Ivanov, B. tenOever, X. Mu, S. Hur, Stress granules are shock absorbers that prevent excessive innate immune responses to dsRNA. *Mol Cell* **83**, 1180–1196.e8 (2023).
24. J. M. Burke, O. C. Ratnayake, J. M. Watkins, R. Perera, R. Parker, G3BP1-dependent condensation of translationally inactive viral RNAs antagonizes infection. *Sci. Adv.* **10**, eadk8152 (2024).
25. Z. Yang, B. A. Johnson, V. A. Meliopoulos, X. Ju, P. Zhang, M. P. Hughes, J. Wu, K. P. Koreski, J. E. Clary, T. C. Chang, G. Wu, J. Hixon, J. Duffner, K. Wong, R. Lemieux, K. G. Lokugamage, R. E. Alvarado, P. A. Crocquet-Valdes, D. H. Walker, K. S. Plante, J. A. Plante, S. C. Weaver, H. J. Kim, R. Meyers, S. Schultz-Cherry, Q. Ding, V. D. Menachery, J. P. Taylor, Interaction between host G3BP and viral nucleocapsid protein regulates SARS-CoV-2 replication and pathogenicity. *Cell Rep.* **43**, 113965 (2024).
26. H. J. Kim, N. C. Kim, Y. D. Wang, E. A. Scarborough, J. Moore, Z. Diaz, K. S. MacLea, B. Freibaum, S. Li, A. Molliex, A. P. Kanagaraj, R. Carter, K. B. Boylan, A. M. Wojtas, R. Rademakers, J. L. Pinkus, S. A. Greenberg, J. Q. Trojanowski, B. J. Traynor, B. N. Smith, S. Topp, A. S. Gkazi, J. Miller, C. E. Shaw, M. Kottlors, J. Kirschner, A. Pestronk, Y. R. Li, A. F. Ford, A. D. Gitler, M. Benatar, O. D. King, V. E. Kimonis, E. D. Ross, C. C. Weihl, J. Shorter, J. P. Taylor, Mutations in prion-like domains in hnRNPA2B1 and hnRNPA1 cause multisystem proteinopathy and ALS. *Nature* **495**, 467–473 (2013).
27. J. R. Buchan, R. M. Kolaitis, J. P. Taylor, R. Parker, Eukaryotic stress granules are cleared by autophagy and Cdc48/VCP function. *Cell* **153**, 1461–1474 (2013).
28. A. Molliex, J. Temirov, J. Lee, M. Coughlin, A. P. Kanagaraj, H. J. Kim, T. Mittag, J. P. Taylor, Phase separation by low complexity domains promotes stress granule assembly and drives pathological fibrillization. *Cell* **163**, 123–133 (2015).
29. I. R. Mackenzie, A. M. Nicholson, M. Sarkar, J. Messing, M. D. Purice, C. Pottier, K. Annu, M. Baker, R. B. Perkerson, A. Kurti, B. J. Matchett, T. Mittag, J. Temirov, G. R. Hsiung, C. Krieger, M. E. Murray, M. Kato, J. D. Fryer, L. Petrucelli, L. Zinman, S. Weintraub, M. Mesulam, J. Keith, S. A. Zivkovic, V. Hirsch-Reinshagen, R. P. Roos, S. Züchner, N. R. Graff-Radford, R. C. Petersen, R. J. Caselli, Z. K. Wszolek, E. Finger, C. Lippa, D. Lacomis, H. Stewart, D. W. Dickson, H. J. Kim, E. Rogaeva, E. Bigio, K. B. Boylan, J. P. Taylor, R. Rademakers, TIA1 mutations in amyotrophic lateral sclerosis and frontotemporal dementia promote phase separation and alter stress granule dynamics. *Neuron* **95**, 808–816.e9 (2017).
30. A. Patel, H. O. Lee, L. Jawerth, S. Maharana, M. Jahnel, M. Y. Hein, S. Stoynov, J. Mahamid, S. Saha, T. M. Franzmann, A. Pozniakovski, I. Poser, N. Maghelli, L. A. Royer, M. Weigert, E. W. Myers, S. Grill, D. Drechsel, A. A. Hyman, S. Alberti, A liquid-to-solid phase transition of the ALS protein FUS accelerated by disease mutation. *Cell* **162**, 1066–1077 (2015).
31. T. Kakihana, M. Takahashi, Y. Katsuragi, S. I. Yamashita, J. Sango, T. Kanki, O. Onodera, M. Fujii, The optineurin/TIA1 pathway inhibits aberrant stress granule formation and reduces ubiquitinated TDP-43. *iScience* **24**, 102733 (2021).
32. Y. R. Li, O. D. King, J. Shorter, A. D. Gitler, Stress granules as crucibles of ALS pathogenesis. *J. Cell Biol.* **201**, 361–372 (2013).
33. S. K. Custer, M. Neumann, H. Lu, A. C. Wright, J. P. Taylor, Transgenic mice expressing mutant forms VCP/p97 recapitulate the full spectrum of IBMPFD including degeneration in muscle, brain and bone. *Hum. Mol. Genet.* **19**, 1741–1755 (2010).
34. T. Kurashige, M. Kuramochi, R. Ohsawa, Y. Yamashita, G. Shioi, H. Morino, M. Kamada, T. Ayaki, H. Ito, Y. Sotomaru, H. Maruyama, H. Kawakami, Optineurin defects cause TDP43-pathology with autophagic vacuolar formation. *Neurobiol. Dis.* **148**, 105215 (2021).
35. M. Badadani, A. Nalbandian, G. D. Watts, J. Vesa, M. Kitazawa, H. Su, J. Tanaja, E. Dec, D. C. Wallace, J. Mukherjee, V. Caiozzo, M. Warman, V. E. Kimonis, VCP associated inclusion body myopathy and paget disease of bone knock-in mouse model exhibits tissue pathology typical of human disease. *PLOS ONE* **5**, e13183 (2010).
36. A. Nalbandian, K. J. Llewellyn, M. Kitazawa, H. Z. Yin, M. Badadani, N. Khanlou, R. Edwards, C. Nguyen, J. Mukherjee, T. Mozaffar, G. Watts, J. Weiss, V. E. Kimonis, The homozygote VCP($R^{155}H/R^{155}H$) mouse model exhibits accelerated human VCP-associated disease pathology. *PLOS ONE* **7**, e46308 (2012).
37. A. Nalbandian, K. J. Llewellyn, M. Badadani, H. Z. Yin, C. Nguyen, V. Katheria, G. Watts, J. Mukherjee, J. Vesa, V. Caiozzo, T. Mozaffar, J. H. Weiss, V. E. Kimonis, A progressive translational mouse model of human valosin-containing protein disease: The VCP($R^{155}H/+$) mouse. *Muscle Nerve* **47**, 260–270 (2013).
38. T. Murakami, S. Qamar, J. Q. Lin, G. S. Schierle, E. Rees, A. Miyashita, A. R. Costa, R. B. Dodd, F. T. Chan, C. H. Michel, D. Kronenberg-Versteeg, Y. Li, S. P. Yang, Y. Wakutani, W. Meadows, R. R. Ferry, L. Dong, G. G. Tartaglia, G. Favrin, W. L. Lin, D. W. Dickson, M. Zhen, D. Ron, G. Schmitt-Ulms, P. E. Fraser, N. A. Shneider, C. Holt, M. Vendruscolo, C. F. Kaminski, P. S. George-Hyslop, ALS/FTD mutation-induced phase transition of FUS liquid droplets and reversible hydrogels into irreversible hydrogels impairs RNP granule function. *Neuron* **88**, 678–690 (2015).
39. C. C. Weihl, P. Temiz, S. E. Miller, G. Watts, C. Smith, M. Forman, P. I. Hanson, V. Kimonis, A. Pestronk, TDP-43 accumulation in inclusion body myopathy muscle suggests a common pathogenic mechanism with frontotemporal dementia. *J. Neurol. Neurosurg. Psychiatry* **79**, 1186–1189 (2008).
40. R. C. Bucelli, K. Arhzaouy, A. Pestronk, S. K. Pittman, L. Rojas, C. M. Sue, A. Evilä, P. Hackman, B. Udd, M. B. Harms, C. C. Weihl, SQSTM1 splice site mutation in distal myopathy with rimmed vacuoles. *Neurology* **85**, 665–674 (2015).
41. G. D. Watts, J. Wymer, M. J. Kovach, S. G. Mehta, S. Mumm, D. Darvish, A. Pestronk, M. P. Whyte, V. E. Kimonis, Inclusion body myopathy associated with Paget disease of bone and frontotemporal dementia is caused by mutant valosin-containing protein. *Nat. Genet.* **36**, 377–381 (2004).
42. H. Maruyama, H. Morino, H. Ito, Y. Izumi, H. Kato, Y. Watanabe, Y. Kinoshita, M. Kamada, H. Nodera, H. Suzuki, O. Komure, S. Matsuura, K. Kobatake, N. Morimoto, K. Abe, N. Suzuki, M. Aoki, A. Kawata, T. Hirai, T. Kato, K. Ogasawara, A. Hirano, T. Takumi, H. Kusaka, K. Hagiwara, R. Kaji, H. Kawakami, Mutations of optineurin in amyotrophic lateral sclerosis. *Nature* **465**, 223–226 (2010).
43. H. X. Deng, W. Chen, S. T. Hong, K. M. Boycott, G. H. Gorrie, N. Siddique, Y. Yang, F. Fecto, Y. Shi, H. Zhai, H. Jiang, M. Hirano, E. Rampersaud, G. H. Jansen, S. Donkervoort, E. H. Bigio, B. R. Brooks, K. Ajroud, R. L. Sufit, J. L. Haines, E. Mugnaini, M. A. Pericak-Vance, T. Siddique, Mutations in UBQLN2 cause dominant X-linked juvenile and adult-onset ALS and ALS/dementia. *Nature* **477**, 211–215 (2011).
44. C. S. Pontifex, M. Zaman, R. D. Fanganiello, T. E. Shutt, G. Pfeffer, Valosin-Containing Protein (VCP): A review of its diverse molecular functions and clinical phenotypes. *Int. J. Mol. Sci.* **25**, 5633 (2024).
45. D. H. Wolf, A. Stolz, The Cdc48 machine in endoplasmic reticulum associated protein degradation. *Biochim. Biophys. Acta* **1823**, 117–124 (2012).
46. N. C. Kim, E. Tresse, R. M. Kolaitis, A. Molliex, R. E. Thomas, N. H. Alami, B. Wang, A. Joshi, R. B. Smith, G. P. Ritson, B. J. Winborn, J. Moore, J. Y. Lee, T. P. Yao, L. Pallanck, M. Kundu, J. P. Taylor, VCP is essential for mitochondrial quality control by PINK1/Parkin and this function is impaired by VCP mutations. *Neuron* **78**, 65–80 (2013).
47. S. M. Hill, L. Wrobel, A. Ashkenazi, M. Fernandez-Estevez, K. Tan, R. W. Bürli, D. C. Rubinsztein, VCP/p97 regulates Beclin-1-dependent autophagy initiation. *Nat. Chem. Biol.* **17**, 448–455 (2021).
48. H. Meyer, C. C. Weihl, The VCP/p97 system at a glance: Connecting cellular function to disease pathogenesis. *J. Cell Sci.* **127**, 3877–3883 (2014).
49. P. Hänzelmann, H. Schindelin, The interplay of cofactor interactions and post-translational modifications in the regulation of the AAA+ ATPase p97. *Front. Mol. Biosci.* **4**, 21 (2017).
50. J. S. Bogan, N. Hendon, A. E. McKee, T. S. Tsao, H. F. Lodish, Functional cloning of TUG as a regulator of GLUT4 glucose transporter trafficking. *Nature* **425**, 727–733 (2003).
51. M. Ladanyi, M. Y. Lui, C. R. Antonescu, A. Krause-Boehm, A. Meindl, P. Argani, J. H. Healey, T. Ueda, H. Yoshikawa, A. Meloni-Ehrig, P. H. Sorensen, F. Mertens, N. Mandahl, H. van den Berghe, R. Sciot, P. Dal Cin, J. Bridge, The der(17)t(X;17)(p11;q25) of human alveolar soft part sarcoma fuses the TFE3 transcription factor gene to ASPL, a novel gene at 17q25. *Oncogene* **20**, 48–57 (2001).
52. A. Arumughan, Y. Roske, C. Barth, L. L. Forero, K. Bravo-Rodriguez, A. Redel, S. Kostova, E. McShane, R. Opitz, K. Faelber, K. Rau, T. Mielke, O. Daumke, M. Selbach, E. Sanchez-Garcia, O. Rocks, D. Panakova, U. Heinemann, E. E. Wanker, Quantitative interaction mapping reveals an extended UBX domain in ASPL that disrupts functional p97 hexamers. *Nat. Commun.* **7**, 13047 (2016).
53. E. N. Habtemichael, D. T. Li, J. P. Camporez, X. O. Westergaard, C. I. Sales, X. Liu, F. López-Giráldez, S. G. DeVries, H. Li, D. M. Ruiz, K. Y. Wang, B. S. Sayal, S. González Zapata, P. Dann, S. N. Brown, S. Hirabara, D. F. Vatner, L. Goedeke, W. Philbrick, G. I. Shulman, J. S. Bogan, Insulin-stimulated endoproteolytic TUG cleavage links energy expenditure with glucose uptake. *Nat. Metab.* **3**, 378–393 (2021).
54. A. Pozner, S. P. Verma, L. Li, S. Wang, J. J. Barrott, M. L. Nelson, J. S. E. Yu, G. L. Negri, S. Colborne, C. S. Hughes, J. F. Zhu, S. L. Lambert, L. S. Carroll, K. Smith-Fry, M. G. Stewart, S. Kannan, B. Jensen, K. L. Mortenson, C. John, S. Sikdar, H. Liu, N. H. Dang, J. Bourdage, J. Li, J. M. Vahrenkamp, J. S. Groundland, R. Wustrack, D. L. Senger, F. J. Zemp, D. J. Mahoney, J. Gertz, X. Zhang, A. J. Lazar, M. Hirst, G. B. Morin, T. O. Nielsen, P. S. Shen, K. B. Jones, ASPSCR1-TFE3 reprograms transcription by organizing enhancer loops around hexameric VCP/p97. *Nat. Commun.* **15**, 1165 (2024).
55. P. Cloutier, M. Lavallée-Adam, D. Faubert, M. Blanchette, B. Coulombe, A newly uncovered group of distantly related lysine methyltransferases preferentially interact with molecular chaperones to regulate their activity. *PLoS Genet.* **9**, e1003210 (2013).
56. R. Rijal, K. Arhzaouy, K. H. Strucksberg, M. Cross, A. Hofmann, R. Schröder, C. S. Clemen, L. Eichinger, Mutant p97 exhibits species-specific changes of its ATPase activity and compromises the UBXD9-mediated monomerisation of p97 hexamers. *Eur. J. Cell Biol.* **95**, 195–207 (2016).

57. W. Shi, R. Ding, Y. Chen, F. Ji, J. Ji, W. Ma, J. Jin, The HRD1-SEL1L ubiquitin ligase regulates stress granule homeostasis in couple with distinctive signaling branches of ER stress. *iScience* **27**, 110196 (2024).
58. N. Kedersha, M. D. Panas, C. A. Achorn, S. Lyons, S. Tisdale, T. Hickman, M. Thomas, J. Lieberman, G. M. McInerney, P. Ivanov, P. Anderson, G3BP-Caprin1-USP10 complexes mediate stress granule condensation and associate with 40S subunits. *J. Cell Biol.* **212**, 845–860 (2016).
59. B. D. Freibaum, J. Messing, P. Yang, H. J. Kim, J. P. Taylor, High-fidelity reconstitution of stress granules and nucleoli in mammalian cellular lysate. *J. Cell Biol.* **220**, (2021).
60. J. Jumper, R. Evans, A. Pritzel, T. Green, M. Figurnov, O. Ronneberger, K. Tunyasuvunakool, R. Bates, A. Žídek, A. Potapenko, A. Bridgland, C. Meyer, S. A. A. Kohl, A. J. Ballard, A. Cowie, B. Romera-Paredes, S. Nikolov, R. Jain, J. Adler, T. Back, S. Petersen, D. Reiman, E. Clancy, M. Zielinski, M. Steinegger, M. Pacholska, T. Berghammer, S. Bodenstein, D. Silver, O. Vinyals, A. W. Senior, K. Kavukcuoglu, P. Kohli, D. Hassabis, Highly accurate protein structure prediction with AlphaFold. *Nature* **596**, 583–589 (2021).
61. A. Ghosh, H. X. Zhou, Determinants for fusion speed of biomolecular droplets. *Angew. Chem. Int. Ed. Engl.* **59**, 20837–20840 (2020).
62. E. Arad, H. Green, R. Jelinek, H. Rapaport, Revisiting thioflavin T (ThT) fluorescence as a marker of protein fibrillation - The prominent role of electrostatic interactions. *J. Colloid Interface Sci.* **573**, 87–95 (2020).
63. I. Alshareedah, M. M. Moosa, M. Pham, D. A. Potoyan, P. R. Banerjee, Programmable viscoelasticity in protein-RNA condensates with disordered sticker-spacer polypeptides. *Nat. Commun.* **12**, 6620 (2021).
64. I. Alshareedah, W. M. Borcherds, S. R. Cohen, A. Singh, A. E. Posey, M. Farag, A. Bremer, G. W. Strout, D. T. Tomares, R. V. Pappu, T. Mittag, P. R. Banerjee, Sequence-specific interactions determine viscoelasticity and ageing dynamics of protein condensates. *Nat. Phys.* **20**, 1482–1491 (2024).
65. C. Mathieu, R. V. Pappu, J. P. Taylor, Beyond aggregation: Pathological phase transitions in neurodegenerative disease. *Science* **370**, 56–60 (2020).
66. J. A. Riback, L. Zhu, M. C. Ferrolino, M. Tolbert, D. M. Mitrea, D. W. Sanders, M. T. Wei, R. W. Kriwacki, C. P. Brangwynne, Composition-dependent thermodynamics of intracellular phase separation. *Nature* **581**, 209–214 (2020).
67. I. Alshareedah, A. Singh, S. Yang, V. Ramachandran, A. Quinn, D. A. Potoyan, P. R. Banerjee, Determinants of viscoelasticity and flow activation energy in biomolecular condensates. *Sci. Adv.* **10**, eadi6539 (2024).
68. J. S. Ju, R. A. Fuentealba, S. E. Miller, E. Jackson, D. Piwnica-Worms, R. H. Baloh, C. C. Weihl, Valosin-containing protein (VCP) is required for autophagy and is disrupted in VCP disease. *J. Cell Biol.* **187**, 875–888 (2009).
69. E. Tresse, F. A. Salomons, J. Vesa, L. C. Bott, V. Kimonis, T. P. Yao, N. P. Dantuma, J. P. Taylor, VCP/p97 is essential for maturation of ubiquitin-containing autophagosomes and this function is impaired by mutations that cause IBMPFD. *Autophagy* **6**, 217–227 (2010).
70. A. S. Dixon, M. K. Schwinn, M. P. Hall, K. Zimmerman, P. Otto, T. H. Lubben, B. L. Butler, B. F. Binkowski, T. Machleidt, T. A. Kirkland, M. G. Wood, C. T. Eggers, L. P. Encell, K. V. Wood, NanoLuc complementation reporter optimized for accurate measurement of protein interactions in cells. *ACS Chem. Biol.* **11**, 400–408 (2016).
71. E. Al-Obeidi, S. Al-Tahan, A. Surampalli, N. Goyal, A. K. Wang, A. Hermann, M. Omizo, C. Smith, T. Mozaffar, V. Kimonis, Genotype-phenotype study in patients with valosin-containing protein mutations associated with multisystem proteinopathy. *Clin. Genet.* **93**, 119–125 (2018).
72. B. Caffrey, X. Zhu, A. Berezuk, K. Tuttle, S. Chittori, S. Subramaniam, AAA+ ATPase p97/VCP mutants and inhibitor binding disrupt inter-domain coupling and subsequent allosteric activation. *J. Biol. Chem.* **297**, 101187 (2021).
73. D. Haubenberger, R. E. Bittner, S. Rauch-Shorny, F. Zimprich, C. Mannhalter, L. Wagner, I. Mineva, K. Vass, E. Auff, A. Zimprich, Inclusion body myopathy and Paget disease is linked to a novel mutation in the VCP gene. *Neurology* **65**, 1304–1305 (2005).
74. J. van der Zee, D. Pirici, T. Van Langenhove, S. Engelborghs, R. Vandenberghe, M. Hoffmann, G. Pusswald, M. Van den Broeck, K. Peeters, M. Mattheijssens, J. J. Martin, P. P. De Deyn, M. Cruts, D. Haubenberger, S. Kumar-Singh, A. Zimprich, C., Clinical heterogeneity in 3 unrelated families linked to VCP p.Arg159His. *Neurology* **73**, 626–632 (2009).
75. M. Koppers, M. M. van Blitterswijk, L. Vlam, P. A. Rowicka, P. W. van Vught, E. J. Groen, W. G. Spliet, J. Engelen-Lee, H. J. Schelhaas, M. de Visser, A. J. van der Kooi, W. L. van der Pol, R. J. Pasterkamp, J. H. Veldink, L. H. van den Berg, VCP mutations in familial and sporadic amyotrophic lateral sclerosis. *Neurobiol. Aging* **33**, 837.e7–837.e13 (2012).
76. W. De Ridder, A. Azmi, C. S. Clemen, L. Eichinger, A. Hofmann, R. Schröder, K. Johnson, A. Töpf, V. Straub, P. De Jonghe, S. Maudsley, J. L. De Bleecker, J. Baets, Multisystem proteinopathy due to a homozygous p.Arg159His VCP mutation: A tale of the unexpected. *Neurology* **94**, e785–e796 (2020).
77. G. Pfeffer, G. Lee, C. S. Pontifex, R. D. Fanganiello, A. Peck, C. C. Weihl, V. Kimonis, Multisystem proteinopathy due to VCP mutations: A review of clinical heterogeneity and genetic diagnosis. *Genes* **13**, 963 (2022).
78. S. Alberti, D. Dormann, Liquid-liquid phase separation in disease. *Annu. Rev. Genet.* **53**, 171–194 (2019).
79. N. B. Nedelsky, J. P. Taylor, Bridging biophysics and neurology: Aberrant phase transitions in neurodegenerative disease. *Nat. Rev. Neurol.* **15**, 272–286 (2019).
80. J. P. Taylor, R. H. Brown Jr., D. W. Cleveland, Decoding ALS: From genes to mechanism. *Nature* **539**, 197–206 (2016).
81. L. McGurk, E. Gomes, L. Guo, J. Mojsilovic-Petrovic, V. Tran, R. G. Kalb, J. Shorter, N. M. Bonini, Poly(ADP-ribose) prevents pathological phase separation of TDP-43 by promoting liquid demixing and stress granule localization. *Mol. Cell* **71**, 703–717.e9 (2018).
82. M. Kar, F. Dar, T. J. Welsh, L. T. Vogel, R. Kühnemuth, A. Majumdar, G. Krainer, T. M. Franzmann, S. Alberti, C. A. M. Seidel, T. P. J. Knowles, A. A. Hyman, R. V. Pappu, Phase-separating RNA-binding proteins form heterogeneous distributions of clusters in subsaturated solutions. *Proc. Natl. Acad. Sci. U.S.A.* **119**, e2202222119 (2022).
83. A. A. Deniz, Percolation physics and density transition frameworks converge in biomolecular condensation. *Proc. Natl. Acad. Sci. U.S.A.* **119**, e2210177119 (2022).
84. B. A. Maxwell, Y. Gwon, A. Mishra, J. Peng, H. Nakamura, K. Zhang, H. J. Kim, J. P. Taylor, Ubiquitination is essential for recovery of cellular activities after heat shock. *Science* **372**, eabc3593 (2021).
85. N. Tolay, A. Buchberger, Comparative profiling of stress granule clearance reveals differential contributions of the ubiquitin system. *Life Sci. Alliance* **4**, e202000927 (2021).
86. M. Weith, J. Seiler, J. van den Boom, M. Kracht, J. Hülsmann, I. Primorac, J. Del Pino Garcia, F. Kaschani, M. Kaiser, A. Musacchio, M. Bollen, H. Meyer, Ubiquitin-independent disassembly by a p97 AAA-ATPase complex drives PP1 holoenzyme formation. *Mol. Cell* **72**, 766–777.e6 (2018).
87. J. van den Boom, G. Marini, H. Meyer, H. R. Saibil, Structural basis of ubiquitin-independent PP1 complex disassembly by p97. *Embo J.* **42**, e113110 (2023).
88. S. Petrović, Y. Roske, B. Rami, M. H. Q. Phan, D. Panáková, U. Heinemann, Structural remodeling of AAA+ ATPase p97 by adaptor protein ASPL facilitates posttranslational methylation by METTL21D. *Proc. Natl. Acad. Sci. U.S.A.* **120**, e2208941120 (2023).
89. T. Q. Nguyen, S. Koh, J. Kwon, S. Jang, W. Kang, J. K. Yang, Structural basis for recognition and methylation of p97 by METTL21D, a valosin-containing protein lysine methyltransferase. *iScience* **26**, 107222 (2023).
90. J. P. Connelly, S. M. Pruett-Miller, CRIS.py: A versatile and high-throughput analysis program for CRISPR-based genome editing. *Sci. Rep.* **9**, 4194 (2019).
91. S. Narina, J. P. Connelly, S. M. Pruett-Miller, High-throughput analysis of CRISPR-Cas9 editing outcomes in cell and animal models using CRIS.py. *Methods Mol. Biol.* **2631**, 155–182 (2023).
92. L. Madsen, K. Molbæk, I. B. Larsen, S. V. Nielsen, E. G. Poulsen, P. S. Walmod, K. Hofmann, M. Seeger, C. Y. Chien, R. H. Chen, F. Kriegenburg, R. Hartmann-Petersen, Human ASPL/TUG interacts with p97 and complements the proteasome mislocalization of a yeast ubx4 mutant, but not the ER-associated degradation defect. *BMC Cell Biol.* **15**, 31 (2014).
93. J. Schindelin, I. Arganda-Carreras, E. Frise, V. Kaynig, M. Longair, T. Pietzsch, S. Preibisch, C. Rueden, S. Saalfeld, B. Schmid, J. Y. Tinevez, D. J. White, V. Hartenstein, K. Eliceiri, P. Tomancak, A. Cardona, Fiji: An open-source platform for biological-image analysis. *Nat. Methods* **9**, 676–682 (2012).
94. P. Jha, X. Wang, J. Auwerx, Analysis of mitochondrial respiratory chain supercomplexes using blue native polyacrylamide gel electrophoresis (BN-PAGE). *Curr. Protoc. Mouse Biol.* **6**, 1–14 (2016).
95. A. Kulesa, M. Krzywinski, P. Blainey, N. Altman, Sampling distributions and the bootstrap. *Nat. Methods* **12**, 477–478 (2015).
96. X. Wang, Y. Li, Z. Wu, H. Wang, H. Tan, J. Peng, JUMP: A tag-based database search tool for peptide identification with high sensitivity and accuracy. *Mol. Cell Proteomics* **13**, 3663–3673 (2014).
97. J. E. Elias, S. P. Gygi, Target-decoy search strategy for increased confidence in large-scale protein identifications by mass spectrometry. *Nat. Methods* **4**, 207–214 (2007).
98. J. Y. Zhou, L. Afjehi-Sadat, S. Asress, D. M. Duong, M. Cudkowicz, J. D. Glass, J. Peng, Galectin-3 is a candidate biomarker for amyotrophic lateral sclerosis: Discovery by a proteomics approach. *J. Proteome Res.* **9**, 5133–5141 (2010).
99. J.-Y. Tinevez, N. Perry, J. Schindelin, G. M. Hoopes, G. D. Reynolds, E. Laplantine, S. Y. Bednarek, S. L. Shorte, K. W. Eliceiri, TrackMate: An open and extensible platform for single-particle tracking. *Methods* **115**, 80–90 (2017).
100. H. Zhao, C. A. Brautigam, R. Ghirlando, P. Schuck, Overview of current methods in sedimentation velocity and sedimentation equilibrium analytical ultracentrifugation. *Curr. Protoc. Protein Sci.*, 10.1002/0471140864.ps2012s71 (2013).
101. P. Schuck, Size-distribution analysis of macromolecules by sedimentation velocity ultracentrifugation and lamm equation modeling. *Biophys. J.* **78**, 1606–1619 (2000).
102. S. K. Chaturvedi, J. Ma, H. Zhao, P. Schuck, Use of fluorescence-detected sedimentation velocity to study high-affinity protein interactions. *Nat. Protoc.* **12**, 1777–1791 (2017).
103. T. M. Laue, B. Shah, T. M. Ridgeway, S. L. Pelletier, in *Analytical Ultracentrifugation in Biochemistry and Polymer Science*, S. E. Harding, A. J. Rowe and J. C. Horton, Eds. (Royal Society of Chemistry, 1992), pp. 90–125.

104. P. H. Brown, P. Schuck, Macromolecular size-and-shape distributions by sedimentation velocity analytical ultracentrifugation. *Biophys. J.* **90**, 4651–4661 (2006).
105. C. A. Brautigam, Calculations and publication-quality illustrations for analytical ultracentrifugation data. *Methods Enzymol.* **562**, 109–133 (2015).

Acknowledgments: We thank V. Pagala and K. Kodali (both of the St. Jude Proteomics and Metabolomics Core), B. Hansen and R. Levine (both of the St. Jude CAGE), and J. Burkhart for technical expertise and assistance. We thank G. Kasof and team at Cell Signaling Technology for generating the antibody against serine-13–phosphorylated VCP. We also thank D. D'Amore, A. McArthur, and N. Nedelsky for editing the manuscript. **Funding:** This work was supported by the National Institutes of Health grants R01 GM132231 and R01 MH115058 (to M.K.), R35 GM138186 (to P.B.), and R35 NS097974 (to J.P.T.); the St. Jude Children's Research Collaborative on the Biology and Biophysics of RNP Granules; and the American Lebanese Syrian Associated Charities (ALSAC). The content is solely the responsibility of the authors and does not necessarily represent the official views of any of the funding bodies. **Author contributions:** Conceptualization: M.K., J.P.T., X.L.-H., R.K., D.L., and B.W. Methodology: R.K., S.M.P.-M., B.D.F., R.D., B.M., T.S.M., A.S., J.P.T., P.B., G.P., D.L., J.L., and X.L.-H. Investigation: G.P., D.L., B.W., J.W., B.D.F., J.L.B., T.S.M., A.S., A.N., H.Q., J.L., X.L.-H., R.K., P.B., and J.M. Validation: G.P., D.L., J.L.B., and R.K. Software: S.P., D.L., A.F.C., and A.S. Formal analysis: G.P., D.L., J.W., J.L.B., A.S., Y.-D.W., A.F.C., Y.N., and S.P. Resources: M.S.R., B.M., X.L.-H., D.L., P.B., and J.P.T. Data curation: D.L., S.P., J.L.B., and P.B. Writing—original draft: M.K., G.P., H.J.K., and D.L. Writing—review and editing: M.K., G.P., H.J.K., D.L., J.W., B.M., S.M.P.-M., A.F.C., M.S.R., J.L.B., X.L.-H., B.W., S.P., and P.B. Visualization: G.P., D.L., J.W., Y.-D.W., and J.L.B. Supervision: S.M.P.-M., H.J.K., R.K., P.B., J.P.T., and M.K. Project administration: D.L., R.K., and P.B. Funding acquisition: M.K., P.B., and J.P.T. **Competing interests:** The authors declare that they have no competing interests. **Data and materials availability:** The raw proteomics data has been deposited to PRIDE repository with the dataset identifier PXD059889 (www.ebi.ac.uk/pride/archive/projects/PXD059889). All other data needed to evaluate the conclusions in the paper are present in the paper and/or the Supplementary Materials.

Submitted 19 April 2025
Accepted 5 September 2025
Published 8 October 2025
10.1126/sciadv.ady3735

ScienceAdvances

ASPL couples the assembly of stress granules with their VCP-mediated disassembly

Gautam Pareek, Dongfang Li, Bo Wang, Jinjun Wu, Brian D. Freibaum, Joseph L. Basalla, Tharun Selvam Mahendran, Anurag Singh, Amanda Nourse, Honghu Quan, Ravi Kalathur, Mitra S. Rana, Brian Maxwell, Yong-Dong Wang, James Messing, Yonghui Ni, Stanley Pounds, Rachayata Dharmat, Jingjun Lu, Xiujie Li-Harms, Alexandre F. Carisey, Shondra M. Pruett-Miller, J. Paul Taylor, Priya Banerjee, Hong Joo Kim, and Mondira Kundu

Sci. Adv. **11** (41), eady3735. DOI: 10.1126/sciadv.ady3735